Efficient and robust stress integration algorithm for anisotropic distortional

hardening law under cross-loading with latent hardening

Jinwoo Lee<sup>1#</sup>, Hyuk Jong Bong<sup>1</sup>, Jinjin Ha<sup>2</sup>

<sup>1</sup>Department of Materials Processing, Korea Institute of Materials Science, Changwon, 51508,

Republic of Korea

<sup>2</sup>Department of Mechanical Engineering, University of New Hampshire, Durham, NH 03824,

**USA** 

# Corresponding author

jwlee0829@kims.re.kr (Jinwoo Lee)

**Abstract** 

A fast and robust stress-update algorithm based on the general cutting-plane method (GCPM)

was developed for a distortional hardening model, known as the HAH-DPS model. It captures

the anisotropic hardening behaviors such as the Bauschinger effect, transient hardening,

differential permanent softening, and cross-loading effects. The lower computational efficiency

of the direct application of GCPM was rectified by considering the all-evolutionary plastic state

variables during iterations. The newly proposed algorithm was formulated on the dependence

of the equivalent plastic strain and the other state variables defined in the distortional hardening

model. And it was implemented in a commercial finite element software using a user-defined

material subroutine (UMAT). Finite element simulations under strain-path change were carried

out to demonstrate the performance of the new numerical algorithm in terms of the convergence

behavior locally as well as globally.

Keywords: Numerical integration; Distortional hardening; Strain-path change; Cross-loading

1

## 1. Introduction

Nowadays, the initial boundary value problems in continuum solid mechanics, characterizing the deformation behavior of the metals, are solved computationally and efficiently by using the finite element method (FEM) (Meng et al., 2018; Seifert and Schmidt, 2008). The robustness of problem solving is highly dependent on the selection of the integration algorithm for computational rate-independent plasticity. Many different numerical algorithms have been proposed to numerically integrate constitutive equations for a given strain increment. As a representative, the radial return-mapping algorithm (called the predictor-corrector algorithm), introduced by Wilkins (Wilkins, 1964), is widely used as the numerical integration algorithm. The return-mapping algorithm follows the operator-splitting methodology, which is the additive splitting of the constitutive equations into the elastic predictor and the subsequent plastic corrector. Then, the new stress is updated iteratively using the plastic corrector projected back to the yield surface. When the projection occurs between the two closest points, it is referred to as the closest-point project method (CPPM). The return mapping algorithm based on CPPM is completely implicit and unconditionally stable; thus, it is used in various applications of elasto-plastic constitutive models (Kim et al., 2008; Ortiz et al., 1983; Ortiz and Popov, 1985).

Despite the advantage of CPPM, the method is mostly suitable for simple plasticity models such as von-Mises plastic yielding with an isotropic hardening law. The Hessian matrix for computing advanced plastic yielding models requires an exceedingly laborious implementation procedure and, as a result, the computation time becomes excessively expensive (Lee et al., 2012; Mánik, 2021). Moreover, for a larger time increment, CPPM tends to diverge; therefore, additional numerical techniques such as line search (Lester and Scherzinger, 2017; Scherzinger, 2017), sub-incrementation (Polat and Dokainish, 1989; Potts and Ganendra, 1994), substepping (Ding et al., 2007; Sloan, 1987), and multi-stage methods (Lee et al., 2015; Yoon et al., 1999a) should be incorporated to overcome these issues (Wissmann and Hauck, 1983). As an alternative, the general cutting-plane method (GCPM) was developed by Ortiz and Simo (Ortiz and Simo, 1986; Simo and Hughes, 1998). Because GCPM is formulated in a frame of the operator-splitting methodology, but with the Newton-Raphson iterative algorithm, it is also an extension of the return-mapping algorithm. However, GCPM does not need to calculate the Hessian matrix (Ghaei et al., 2010; Ortiz and Popov, 1983), which consequently, makes the

implementation of the complex material models in an FEM code simple and efficient (Cardoso and Yoon, 2009; Lee et al., 2005; Safaei et al., 2015).

Various advanced constitutive equations have been developed to reproduce complex material behavior during metal forming processes (Rauch, 1997; Rauch et al., 2002). For example, anisotropic hardening behaviors such as the Bauschinger effect (Hahm and Kim, 2008; Kim and Yin, 1997), transient hardening (Kim and Yin, 1997; Tarigopula et al., 2009), permanent softening (Sun and Wagoner, 2013), and cross-loading behaviors (Ha et al., 2013; Tarigopula et al., 2008) are clearly observed for sheet metals upon strain-path change, and it is necessary to predict these phenomena in the FE analysis for robust and efficient modeling (Choi et al., 2006). In the literature, significant efforts in model development have been devoted to the accurate prediction of anisotropic hardening behaviors, using non-isotropic concepts such as yield-surface-translation (Chaboche, 1986; Geng and Wagoner, 2002; Lee et al., 2007), multiple yield surfaces (Peeters et al., 2001b, 2001a), and microstructural-based model (Hu et al., 1992; Teodosiu and Hu, 1995). Modeling of the yield surface distortion was initially proposed by Baltov and Sawczuk (1965), and the model was formulated via structural tensors, which were functions of the plastic strains. Several models for the extension of their approach have been developed in the literatures. For examples, simple models without the evolution of the back-stress were developed by Feigenbaum and Dafalias (2008, 2007), and Noman et al. (2010) proposed the special case of the distortional model for cross-hardening. The comparison among the different distortional models could be found in literature (Shi and Mosler, 2013). In particular, material models, based on the yield-surface-distortional concept have been recently introduced by Barlat et al. (Barlat et al., 2014, 2011; Butuc et al., 2019), which is referred to as the homogeneous-yield-function-based anisotropic hardening (HAH) model. Extensive validation has been performed on HAH models regarding the anisotropic hardening behaviors under various strain-path changes (Lee et al., 2020; Wi et al., 2020). More recently, a modified version of the HAH model was proposed to describe differential permanent softening, namely HAH-DPS (Homogeneous-yield-function-based anisotropic hardening-Differential permanent softening), with respect to the loading directions (Lee et al., 2020).

With regard to the implementation of the HAH model series into FE codes, the radial return-mapping algorithms, either CPPM or GCPM, for stress-update were utilized by Lee et al. (2012). They developed numerical formulations of the HAH model series using both CPPM

and GCPM (J. Lee et al., 2012), and GCPM with a sub-stepping scheme was proposed to avoid inaccurate solutions owing to the semi-explicit nature of the GCPM (Lee et al., 2015). A multistep return-mapping algorithm based on the CPPM for the HAH model was proposed by Choi and Yoon (Choi and Yoon, 2019), in which the finite difference method was introduced to calculate the first and second derivatives of the distortional yield function. It was also reported that the numerical accuracy of the CPPM for the recent HAH model can be improved by applying the line search method (Lee et al., 2021; Yoon et al., 2020). Recently, Choi et al. (Choi et al., 2021) proposed a fully implicit numerical algorithm that can solve a complete set of residuals, including stress, equivalent plastic strain, and all the plastic state variables of the constitutive model. However, the above studies focused on obtaining a solution for a given strain increment locally. In other words, the global assessment of the tangent operator to obtain a solution to the nonlinear boundary-value problem has not been performed in an implicit FE code. As reported in the literature (Meier et al., 2016; Starman et al., 2014), the tangent operator is necessary to ensure computational efficiency and fast convergence in a global equilibrium; however, a lack of studies on global convergence is observed for the advanced distortional hardening law.

The primary purpose of this study is to evaluate the newly proposed numerical algorithm based on GCPM, locally as well as globally, considering the all-evolutionary plastic state variables of the distortional hardening model in an FE analysis in terms of the computational speed and convergence. Section 2 presents a summary of the distortional hardening model HAH-DPS. Section 3 presents a brief description of the general stress-update algorithm, that includes the computation of the solution given a strain increment and continuum tangent operator. Moreover, the stress-update scheme based on GCPM is reformulated for the distortional hardening model, which considers the evolutionary plastic state variables of the material modeling. As a result, the continuum tangent operator is newly derived with all the components of the model, which affects the convergence behavior in a global equilibrium. Section 4 presents the performance of the two stress-integration algorithms in terms of computation time and convergence behavior by considering two case study simulations. Finally, the conclusions and summary of this study are presented in section 5.

## 2. Theoretical background

## 2.1. Modeling for anisotropic hardening behaviors under strain-path change

The HAH model herein is based on a homogeneous function of the first degree with respect to the Cauchy stress,  $\Phi(\eta \sigma) = \eta \cdot \Phi(\sigma)$ , and it utilizes a distortional hardening concept proposed by Barlat et al. (Barlat et al., 2014, 2013, 2011) to describe anisotropic hardening behaviors, instead of the kinematic hardening concept. The mathematical expression is as follows:

$$\Phi(\mathbf{\sigma}, f_1, f_2, \hat{\mathbf{h}}^{\mathbf{s}}) = \left\{ \varphi^{\mathbf{q}}(\mathbf{\sigma}) + \varphi_{\mathbf{h}}(\mathbf{\sigma}, f_1, f_2, \hat{\mathbf{h}}^{\mathbf{s}}) \right\}^{\frac{1}{\mathbf{q}}} = \bar{\sigma}_{\mathrm{IH}}(\bar{\epsilon}), \tag{1}$$

where  $\Phi$  is the equivalent stress,  $\sigma$  is the Cauchy stress, s is the deviatoric stress tensor, the function  $\varphi$  is the stable component that represents the material anisotropic property, and  $\varphi_h$  is the fluctuating component that controls the distortion of the yield surface. The exponent q is the material constant for controlling the sharpness of the distorted yield surface,  $\bar{\epsilon}$  is the equivalent plastic strain, and  $\bar{\sigma}_{IH}$  is the reference flow hardening curve to be fitted by the Swift hardening law,  $\bar{\sigma}_{IH} = C \cdot (\bar{\epsilon} + \epsilon_0)^n$ , and C and  $\epsilon_0$  are the material coefficients to be identified from the flow curve of the uniaxial tension. Notably,  $\bar{\sigma}_{IH}$  can replace any equivalent expressions for reference flow hardening.  $\hat{\mathbf{h}}^s$  is a special tensor, namely the microstructure deviator, introduced to hold the material deformation history and determine the direction of the yield surface distortion. The hat symbol above  $\mathbf{h}$  indicates that the quantity of the deviator is normalized as  $\hat{x}_{ij} = x_{ij} / \sqrt{8/3 \cdot x_{ij} x_{ij}}$ , and its initial component is the same as the deviatoric stress  $\mathbf{s}$  when the first plastic deformation occurs.

The Bauschinger effect, transient hardening, and differential permanent softening behaviors can be successfully reproduced by the distortion of the yield surface, controlled by the state variables  $f_1$  and  $f_2$  in Eq. (1) of the fluctuating component  $\varphi_h$ . The two state variables  $f_1$  and  $f_2$  are additionally expressed using the plastic state variables  $g_1$  and  $g_2$ , and the fluctuating component  $\varphi_h$  is defined as follows:

$$\varphi_{\mathbf{h}}(\mathbf{\sigma}, f_1, f_2, \hat{\mathbf{h}}^{\mathbf{s}}) = f_1^{\mathbf{q}} \left| \hat{\mathbf{h}}^{\mathbf{s}} : \mathbf{s} - \left| \hat{\mathbf{h}}^{\mathbf{s}} : \mathbf{s} \right| \right|^{\mathbf{q}} + f_2^{\mathbf{q}} \left| \hat{\mathbf{h}}^{\mathbf{s}} : \mathbf{s} + \left| \hat{\mathbf{h}}^{\mathbf{s}} : \mathbf{s} \right| \right|^{\mathbf{q}}$$
(2)

$$f_{k} = \left[\frac{1}{g_{k}^{q}} - 1\right]^{1/q}$$
, and  $k = 1, 2$ . (3)

Here, ":" symbol represents the double dot product of the second-order tensors A and B (will be omitted) defined as:

$$\mathbf{A} : \mathbf{B} = (a_{ij} \mathbf{e}_{i} \otimes \mathbf{e}_{j}) : (b_{kl} \mathbf{e}_{k} \otimes \mathbf{e}_{l}) = a_{ij} b_{kl} \delta_{ik} \delta_{il}, \tag{4}$$

where  $\delta_{ik}$  and  $\delta_{jl}$  are Kronecker delta function. And the frame  $e_m$  (m = 1, 2, 3) represents a fixed orthonormal coordinate system.

The evolution laws for the state variables in the HAH-DPS model are formulated with an equivalent plastic strain and are given as

$$\frac{\mathrm{d}g_{i}}{\mathrm{d}\bar{\epsilon}} = k_{2} \left( k_{3} \frac{\bar{\sigma}_{\mathrm{IH}}(0)}{\bar{\sigma}_{\mathrm{IH}}(\bar{\epsilon})} - g_{i} \right) \tag{5}$$

$$\frac{\mathrm{d}g_{\mathrm{j}}}{\mathrm{d}\bar{\epsilon}} = k_{1} \frac{\left[g_{\mathrm{k}} + (1 - g_{\mathrm{k}})(1 - \cos^{2}\omega) - g_{\mathrm{j}}\right]}{g_{\mathrm{j}}}$$
 (6)

$$\frac{\mathrm{d}g_1}{\mathrm{d}\bar{s}} = k_5 (k_4 - g_1),\tag{7}$$

$$\frac{d\hat{\mathbf{h}}^{s}}{d\bar{\epsilon}} = k \cdot \text{sgn}(\cos \chi) \left[ |\cos \chi|^{1/z} + g_{R} \right] (\hat{\mathbf{s}} - \cos \chi \hat{\mathbf{h}}^{s}), \tag{8}$$

where  $k_1-k_5$  are material constants and subscripts (i, j, k, l) are (1, 2, 3, 4) or (2, 1, 4, 3) if  $\hat{\mathbf{h}}^s : \mathbf{s} \ge 0$  or  $\hat{\mathbf{h}}^s : \mathbf{s} < 0$ , respectively. The function sgn(.), the scalar parameters  $\cos \omega$  (J. Lee et al., 2020) and  $\cos \chi$  (Schmitt et al., 1994), and the evolution law of the state variable  $g_R$  are given by:

$$\cos \chi = \frac{8}{3} (\hat{\mathbf{s}}_{L} : \hat{\mathbf{h}}^{s}), \tag{9}$$

$$\operatorname{sgn}(\mathbf{x}) = \begin{cases} 1 & \text{if } \mathbf{x} \ge 0 \\ -1 & \text{if } \mathbf{x} < 0 \end{cases} \text{ and } \frac{\operatorname{d}\mathbf{g}_{R}}{\operatorname{d}\bar{\epsilon}} = k_{R} \left[ k_{R} (1 - \cos^{2} \chi) - g_{R} \right], \tag{10}$$

$$\cos \omega = \frac{8}{3} \frac{\hat{\mathbf{s}}_0 : \hat{\mathbf{s}}_L}{|\hat{\mathbf{s}}_0| |\hat{\mathbf{s}}_L|},\tag{11}$$

where  $\hat{\mathbf{s}}_0$  and  $\hat{\mathbf{s}}_L$  are the stress deviators corresponding to the first plastic strain increment and current plastic deformation, respectively. In the above evolution laws, z = 5,  $k_R = 15$ , and  $k_R' = 0.2$  are suggested values.

Cross-loading behaviors, either cross-hardening or cross-softening under cross-loading paths, are modeled using additional functions in the stable component  $\varphi$  of Eq. (1) with state variables as follows:

$$\varphi(\mathbf{s}) = \sqrt{\psi(\mathbf{s})^2 + \psi(\mathbf{s}_p)^2} \text{ with } \psi(\mathbf{s}) = \xi(\mathbf{s}'') \text{ and } \psi(\mathbf{s}_p)$$
 (12)

$$\mathbf{s}'' = \mathbf{s_c} + \eta \mathbf{s_o} \text{ with } \eta = \frac{1}{g_L}$$
 (13)

$$\mathbf{s_p} = 4(1 - g_S)\mathbf{s_o},\tag{14}$$

where  $\mathbf{s_c}$  and  $\mathbf{s_o}$  are decomposed stress tensors collinear and orthogonal to the microstructure deviator  $\hat{\mathbf{h}}^s$ , defined as  $\mathbf{s_c} = \frac{8}{3} \ (\mathbf{s:\hat{h}}^s) \ \hat{\mathbf{h}}^s$  and  $\mathbf{s_o} = \mathbf{s} - \mathbf{s_c}$ , respectively. The function  $\xi$  can be any isotropic or anisotropic yield function.

The state variables  $g_L$  and  $g_S$  control the description of cross-hardening and cross-softening under the given cross-loading condition, respectively, and their evolution laws during plastic deformation are defined as follows:

$$\frac{\mathrm{d}g_{\mathrm{L}}}{\mathrm{d}\bar{\epsilon}} = k_{\mathrm{L}} \left[ \left( 1 - \frac{\bar{\sigma}_{\mathrm{IH}}(0)}{\bar{\sigma}_{\mathrm{IH}}(\bar{\epsilon})} \right) \left( \sqrt{\mathrm{L}(1 - \cos^2\chi) + \cos^2\chi} - 1 \right) + 1 - g_{\mathrm{L}} \right],\tag{15}$$

$$\frac{\mathrm{d}g_{\mathrm{S}}}{\mathrm{d}\bar{\epsilon}} = k_{\mathrm{S}} [1 + (\mathrm{S} - 1)\cos^2 \chi - g_{\mathrm{S}}],\tag{16}$$

where  $k_L$ ,  $k_S$ , S, and L are the material constants.

# 2.2. Graphical interpretation of the HAH-DPS model

As formulated in previous section, the HAH-DPS model can predict the anisotropic hardening behaviors such as the Bauschinger effect, cross-loading effect, and differential permanent softening effect when the loading path changes. Figure 1 (a) and (b) show the yield loci evolution for the latent hardening and cross-loading contraction predicted by the HAH-DPS model under the orthogonal loading condition, respectively. The uniaxial tension in the rolling direction (RD) was prescribed to the material as the first loading (See red dotted surfaces). As shown in figures, the opposite part of the yield locus was distorted to reproduce the Bauschinger effect. Then, as the second loading path, subsequent uniaxial tension along the transverse direction (TD) was subjected (See black lined surfaces). As shown in figures, both distorted yield loci recover the yield locus of the isotropic hardening (Blue dotted surface) to describe the transient and permanent softening, and they are controlled by the state variables g<sub>1-4</sub>. For the latent hardening case, sudden expansion of the yield locus is obtained by using the state variable g<sub>L</sub> during the second loading as described in Figure 1 (a). And the state variable g<sub>S</sub> affects the sudden contraction of the yield locus to reproduce the cross-loading contraction under the orthogonal loading condition as shown in Figure 1 (b).

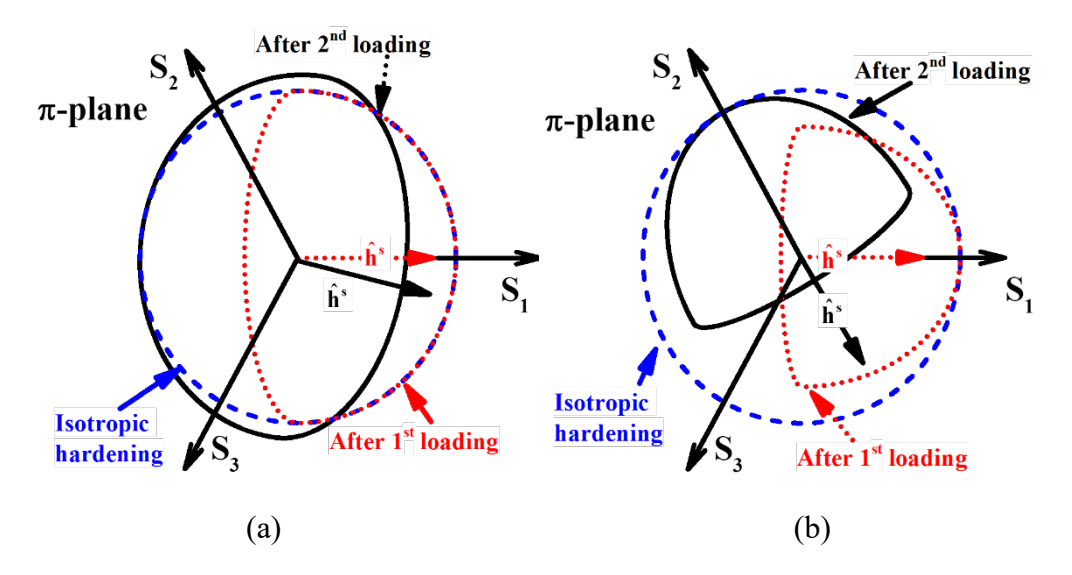


Figure 1: Yield loci prediction of the HAH-DPS model reproducing (a) latent hardening and (b) cross-contraction after pre-tension in RD followed by uniaxial tension in TD (J. Lee et al., 2020).

Figure 2 shows the evolution of the state variable  $g_1$  under two different loading path change conditions; (a) Uniaxial compression in RD followed by the subsequent tension in RD, corresponding to  $\cos \omega = -1$ ; (b) Uniaxial tension in RD followed by the succeeding tension in TD, corresponding to  $\cos \omega = -0.5$ . The state variables  $g_1$  affects the amount of the recovery during the second loading, reproducing the permanent softening effect. As shown in figure, the original HAH model can reproduce the permanent softening effect for two strain-path change conditions while different amount of the permanent softening effect for the HAH-DPS model can be observed. This is because the new state variable  $\cos \omega$  in Eq. (6) influences the evolution of the state variable  $g_1$ , leading to the different predictions for the permanent softening under strain-path changes.

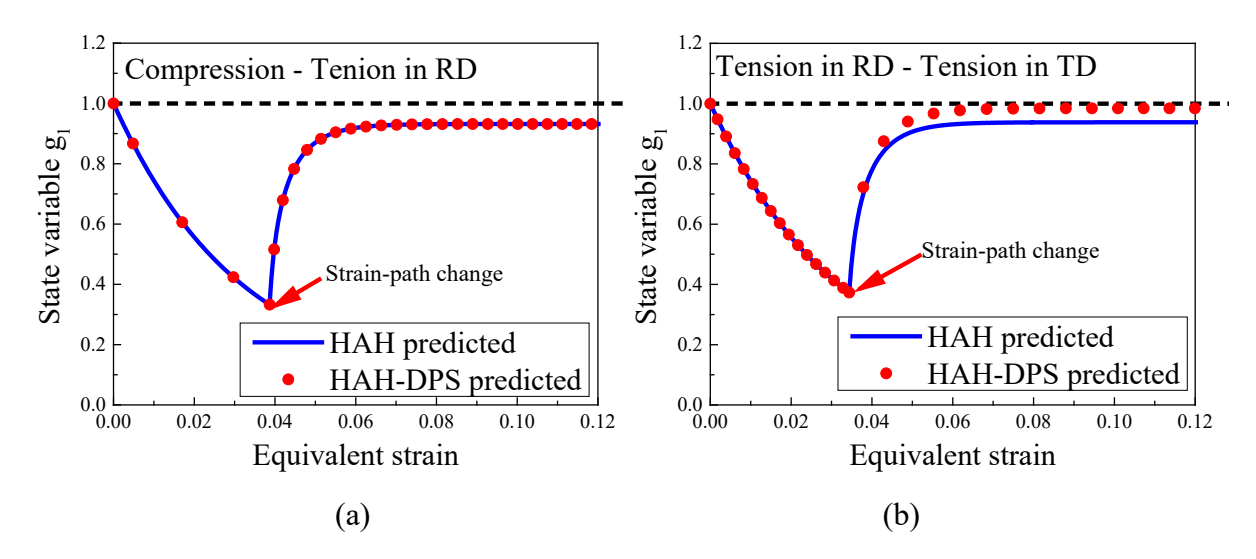


Figure 2: Evolution of the state variable  $g_1$  using the HAH and HAH-DPS models under the strain-path change conditions: (a)  $\cos \omega = -1$  and (b)  $\cos \omega = -0.5$ . The data refer to Lee et al. (J. Lee et al., 2020).

# 3. Numerical implementation for anisotropic distortional hardening

### 3.1. Review of incremental deformation theory

The incremental constitutive equation has been obtained from the minimum plastic work path (Chung and Richmond, 1993, 1992; Yoon et al., 1999a) based on the materially embedded coordinate system. Here, summary of the incremental deformation theory is provided. Let us define the deformation gradient **F**, which describes a deformation between the current time t and the reference time t<sub>0</sub>, and it is decomposed as follows:

$$\mathbf{F}(t) = \mathbf{R}(t)\mathbf{U}(t) \text{ for } t_0 \le t \le t_0 + \Delta t , \qquad (17)$$

where **R** and **U** are rotational and right-stretch tensors in the incremental quantity, respectively.

Considering the relationship for the rate of the deformation tensor  $\mathbf{L} = \mathbf{D} + \mathbf{W} = \dot{\mathbf{F}}\mathbf{F}^{-1}$  ( $\dot{\mathbf{F}} = \partial \mathbf{F}/\partial \mathbf{t}$  and  $\mathbf{F}^{-1} = \mathbf{U}^{-1}\mathbf{R}^{-1}$ ), the deformation rate tensor  $\mathbf{D}$  and the spin tensor  $\mathbf{W}$  are expressed as follows:

$$\mathbf{D} = (\dot{\mathbf{F}}\mathbf{F}^{-1})_{s} = (\mathbf{R}\dot{\mathbf{U}}\mathbf{U}^{-1}\mathbf{R}^{-1})_{s} \text{ and } \mathbf{W} = (\dot{\mathbf{F}}\mathbf{F}^{-1})_{a} = \dot{\mathbf{R}}\mathbf{R}^{-1} + (\mathbf{R}\dot{\mathbf{U}}\mathbf{U}^{-1}\mathbf{R}^{-1})_{a}$$
(18)

where  $\dot{\mathbf{U}}=\partial\mathbf{U}/\partial t$ ,  $\dot{\mathbf{R}}=\partial\mathbf{R}/\partial t$ , and the subscript 'a' and 's' denote the anti-symmetric part and the symmetric part of the tensor, respectively. When the same principal material lines are kept constant during deformation, the following relationships are obtained:

$$\mathbf{D} = \mathbf{R}\dot{\mathbf{U}}\mathbf{U}^{-1}\mathbf{R}^{\mathrm{T}} \tag{19}$$

where  $\mathbf{R}^{T}$  represents the transpose tensor of the tensor  $\mathbf{R}$ . Therefore, the deformation and rotation are conveniently decoupled by using the tensors  $\mathbf{R}$  and  $\mathbf{U}$ .

The objectivity rule is satisfied for the updated stresses, which are rotated by  $\mathbf{R}$ , because the material is rotated by the incremental angle calculated by the polar decomposition at each discrete step.

An invariant quantity with respect to the rotation,  $\hat{\mathbf{D}}$ , is defined as

$$\widehat{\mathbf{D}} = \mathbf{R}^{\mathrm{T}} \mathbf{D} \mathbf{R} = \dot{\mathbf{U}} \mathbf{U}^{-1}. \tag{20}$$

Note that the symbol "^" represents the quantity with respect to the materially embedded

coordinate system or the Lagrangian quantity.

The incremental logarithmic strain quantity at a given time increment is obtained, which satisfies the minimum plastic work condition, as express:

$$\Delta \varepsilon = \int_{t_0}^{t_0 + \Delta t} \widehat{\mathbf{D}} dt = \ln \mathbf{U}(t_0 + \Delta t)$$
 (21)

Note that Eq. (21) is consistent with the rotation neutralized strain tensor of Nagtegaal and Rebelo (1988). And, the total deformation could be decomposed as (Lee, 1969)

$$\mathbf{F} = \mathbf{F}^e \mathbf{F}^p = (\mathbf{R}^e \mathbf{U}^e)(\mathbf{R}^p \mathbf{U}^p) \text{ and } \mathbf{L} = \dot{\mathbf{F}}^e (\mathbf{F}^e)^{-1} + \mathbf{F}^e \dot{\mathbf{F}}^p (\mathbf{F}^p)^{-1} (\mathbf{F}^e)^{-1}$$
 (22)

where the superscripts "e" and "p" mean the elastic and plastic deformations, respectively.

The following relationship is derived for infinitesimal elastic strains (i.e.,  $\mathbf{F}^e \cong \mathbf{I}$ ),

$$\widehat{\mathbf{D}} = \widehat{\mathbf{D}}^e + \widehat{\mathbf{D}}^p. \tag{23}$$

Finally, the incremental logarithmic strain can be decomposed into as follows:

$$\Delta \mathbf{\varepsilon} = \Delta \mathbf{\varepsilon}^e + \Delta \mathbf{\varepsilon}^p \tag{24}$$

where  $\Delta \mathbf{\varepsilon}^e$  and  $\Delta \mathbf{\varepsilon}^p$  are the elastic and plastic strain increments, respectively.

Note that the  $\Delta \varepsilon^e$  is the proportional to the increment of Cauchy stress  $\Delta \sigma$  in the incremental deformation theory. The incremental application of elastic-plasticity for FEM analysis will be introduced in the next section.

## 3.2. Review of the general cutting-plane algorithm

The stress-integration algorithm based on the cutting plane method updates the Cauchy stress  $\sigma$  and the relevant state variables of the material models, at the current time step  $t_{n+1}$  for a given strain increment  $\Delta \varepsilon_{n+1}$ . The proposed cutting plane algorithm is formulated with the Newton–Raphson iteration (Ortiz and Simo, 1986), in which the iteration begins by calculating the elastic predictor. For the simplicity, the proposed algorithmic approach in this study is to

integrate the equivalent plastic strain iteratively but the state variables of the HAH-DPS model explicitly, which are dependent on the equivalent plastic strain.

Assuming that a given strain increment  $\Delta \varepsilon_{n+1}$  is a fully elastic strain increment, the elastic predictor  $\sigma^T$  is computed as follows:

$$\mathbf{\sigma}^{\mathrm{T}} = \mathbf{\sigma}_{\mathrm{n}} + \mathbf{C}^{\mathrm{e}} : \Delta \mathbf{\varepsilon}_{\mathrm{n+1}} , \qquad (25)$$

where  $\sigma_n$  is the Cauchy stress at the previous time step  $t_n$ ,  $C^e$  is the fourth-order isotropic elasticity stiffness tensor, and ":" denotes a tensor product between the fourth-order and second-order tensors defined as:

$$\mathbf{C} : \mathbf{D} = (c_{ijkl} \mathbf{e}_{i} \otimes \mathbf{e}_{j} \otimes \mathbf{e}_{k} \otimes \mathbf{e}_{l}) : (d_{mn} \mathbf{e}_{m} \otimes \mathbf{e}_{n}) = c_{ijkl} d_{mn} \delta_{km} \delta_{ln} \mathbf{e}_{i} \otimes \mathbf{e}_{j}, \quad (26)$$

where  $\delta_{km}$  and  $\delta_{ln}$  are Kronecker delta function. And, the state variables and equivalent plastic strain in the HAH-DPS model are the same as those at the previous time step.

If the following condition is satisfied, the trial stress is purely elastic.

$$\Theta_{n+1}(\boldsymbol{\sigma}^{T}, \bar{\varepsilon}_{n}) = \Phi_{n+1}(\boldsymbol{\sigma}^{T}) - \bar{\sigma}_{IH}(\bar{\varepsilon}_{n}) \leq 0, \qquad (27)$$

where  $\Theta$  determines the plastic yielding of the material, and  $\Phi$  and  $\bar{\sigma}_{IH}$  are defined in Eq. (1). The condition where Eq. (27) holds is denoted as the consistency condition: Then, the updated stress  $\sigma_{n+1}$  at the current step is the trial stress  $\sigma^T$ , and the equivalent strain and other state variables of the HAH-DPS model are kept as the converged values from the previous time step.

However, the material deformation becomes plastic when  $\Theta_{n+1}(\sigma^T, \bar{\epsilon}_n)>0$ . Subsequently, the consistency condition in Eq. (28) is iteratively solved using the unknown variable  $\Delta \gamma$ , which is the incremental plastic multiplier. By applying the associated flow rule and Euler's theorem, the relationship between the equivalent plastic strain increment  $\Delta \bar{\epsilon}$  and plastic multiplier  $\Delta \gamma$  is obtained as follows:

$$\Theta_{n+1} = \Phi(\sigma_n + \Delta \sigma_{n+1}) - \bar{\sigma}_{IH}(\bar{\varepsilon}_n + \Delta \gamma) = \Phi(\sigma_{n+1}) - \bar{\sigma}_{IH}(\bar{\varepsilon}_n + \Delta \bar{\varepsilon}_{n+1}), \tag{28}$$

$$\Delta \mathbf{\varepsilon}^p = \Delta \gamma \frac{\partial \Phi}{\partial \mathbf{\sigma}},\tag{29}$$

$$\Delta \bar{\varepsilon} = \frac{\sigma \Delta \varepsilon^p}{\Phi(\sigma)} = \frac{\sigma \Delta \gamma \frac{\partial \Phi}{\partial \sigma}}{\Phi(\sigma)} = \Delta \gamma \frac{\Phi(\sigma)}{\Phi(\sigma)} = \Delta \gamma , \tag{30}$$

where  $\Delta \varepsilon^p$  is the plastic strain increment.

By applying Taylor's expansion to Eq. (28), the variation of the equivalent plastic strain increment at the (k+1)<sup>th</sup> iteration is as follows:

$$\Delta \bar{\varepsilon}_{n+1}^{(k+1)} = \Delta \bar{\varepsilon}_{n+1}^{k} + \delta(\Delta \bar{\varepsilon}) \text{ and } \Theta_{n+1} \left( \Delta \bar{\varepsilon}_{n+1}^{k} \right) + \frac{\partial \Theta_{n+1} \left( \Delta \bar{\varepsilon}_{n+1}^{k} \right)}{\partial \Delta \bar{\varepsilon}} \delta(\Delta \bar{\varepsilon}) = 0, \tag{31}$$

$$\delta(\Delta \gamma) = \delta(\Delta \bar{\varepsilon}) = -\Theta_{n+1} \left( \Delta \bar{\varepsilon}_{n+1}^{k} \right) / \frac{\partial \Theta_{n+1} \left( \Delta \bar{\varepsilon}_{n+1}^{k} \right)}{\partial \Delta \bar{\varepsilon}}$$

$$= \frac{\Theta_{n+1} \left( \Delta \bar{\varepsilon}_{n+1}^{k} \right)}{\left( \frac{\partial \Phi_{n+1}^{k}}{\partial \sigma_{n+1}^{k}} : C^{e} : \frac{\partial \Phi_{n+1}^{k}}{\partial \sigma_{n+1}^{k}} + H'(\Delta \bar{\varepsilon}_{n+1}^{k}) \right)}, \tag{32}$$

where H' is the slope of the strain-hardening curve, given by the Swift hardening law. The newly updated stress and equivalent plastic strain are computed as

$$\mathbf{\sigma}_{n+1}^{(k+1)} = \mathbf{\sigma}_{n+1}^{k} + \delta(\Delta \overline{\epsilon}) \mathbf{C}^{e} : \frac{\partial \Phi_{n+1}^{k}}{\partial \mathbf{\sigma}_{n+1}^{k}} \text{ and } \overline{\epsilon}_{n+1}^{(k+1)} = \overline{\epsilon}_{n+1}^{k} + \Delta \overline{\epsilon}_{n+1}^{(k+1)}.$$
 (33)

The state variables of the HAH-DPS model are updated at the  $(k+1)^{th}$  iteration as below.

$$\cos \omega = \frac{8}{3} \frac{\hat{\mathbf{s}}_0 : \hat{\mathbf{s}}_L^{(k+1)}}{|\hat{\mathbf{s}}_0| |\hat{\mathbf{s}}_L^{(k+1)}|'}$$
(34)

$$\hat{\mathbf{h}}^{\mathbf{s}(k+1)} = \hat{\mathbf{h}}^{\mathbf{s}(k)} + k \cdot \operatorname{sgn}(\cos \chi) \left[ \left| \cos \chi \right|^{1/z} + g_{R} \right] \left( \hat{\mathbf{s}}^{(k)} - \cos \chi \, \hat{\mathbf{h}}^{\mathbf{s}(k)} \right) \delta(\Delta \bar{\epsilon}), \tag{35}$$

$$\cos \chi = \frac{8}{3} \left( \hat{\mathbf{s}}_{L}^{(k+1)} : \hat{\mathbf{h}}^{s(k+1)} \right), \tag{36}$$

$$g_0^{(k+1)} = g_0^{(k)} + k_2 \left( k_3 \frac{\overline{\sigma}_{IH}(0)}{\overline{\sigma}_{IH}(\overline{\varepsilon}_{n+1}^{(k+1)})} - g_0^{(k)} \right) \delta(\Delta \overline{\varepsilon}), \tag{37}$$

$$g_{p}^{(k+1)} = g_{p}^{(k)} + k_{1} \frac{\left[g_{q} + \left(1 - g_{q}\right)(1 - \cos^{2}\omega) - g_{p}\right]}{g_{p}} \delta(\Delta \bar{\epsilon}),$$
 (38)

$$\mathbf{g}_{r}^{(k+1)} = \mathbf{g}_{r}^{(k)} + \mathbf{k}_{5} (\mathbf{k}_{4} - \mathbf{g}_{r}) \delta(\Delta \bar{\varepsilon}), \text{ for } (\mathbf{0}, \mathbf{p}, \mathbf{q}, \mathbf{r}) \begin{cases} (1, 2, 3, 4) & \hat{\mathbf{h}}^{\mathbf{s}(k+1)} : \mathbf{s}^{(k+1)} \ge 0, \\ (2, 1, 3, 4) & \hat{\mathbf{h}}^{\mathbf{s}(k+1)} : \mathbf{s}^{(k+1)} < 0, \end{cases}$$
(39)

$$\begin{split} g_L^{(k+1)} &= g_L^{(k)} + k_L \left[ \left( 1 - \frac{\overline{\sigma}_{IH}(0)}{\overline{\sigma}_{IH}(\overline{\epsilon}_{n+1}^{(k+1)})} \right) \left( \sqrt{L(1 - \cos^2\chi) + \cos^2\chi} - 1 \right) + 1 \right. \\ &\left. - g_L \right] \delta(\Delta \overline{\epsilon}), \end{split} \tag{40}$$

$$g_S^{(k+1)} = g_S^{(k)} + k_S [1 + (S-1)\cos^2 \chi - g_S] \delta(\Delta \overline{\epsilon}), \tag{41}$$

$$g_R^{(k+1)} = g_R^{(k)} + k_R [k_R'(1 - \cos^2 \chi) - g_R] \delta(\Delta \bar{\epsilon}),$$
 (42)

The iterations are terminated upon satisfying the following criteria:

$$\Gamma = \frac{\left|\Theta\left(\Delta \bar{\varepsilon}_{n+1}^{(k+1)}\right)\right|}{\bar{\sigma}_{IH}\left(\bar{\varepsilon}_{n+1}^{(k+1)}\right)} < \text{Tol}$$
(43)

where the tolerances used in this study is  $Tol = 10^{-6}$ .

Figure 3 shows a schematic of the proposed numerical algorithm. As shown in the figure, the updated stress at the (k+1)<sup>th</sup> iteration is returned along with the tangent cut of the yield surface at the stress point of the k<sup>th</sup> iteration.

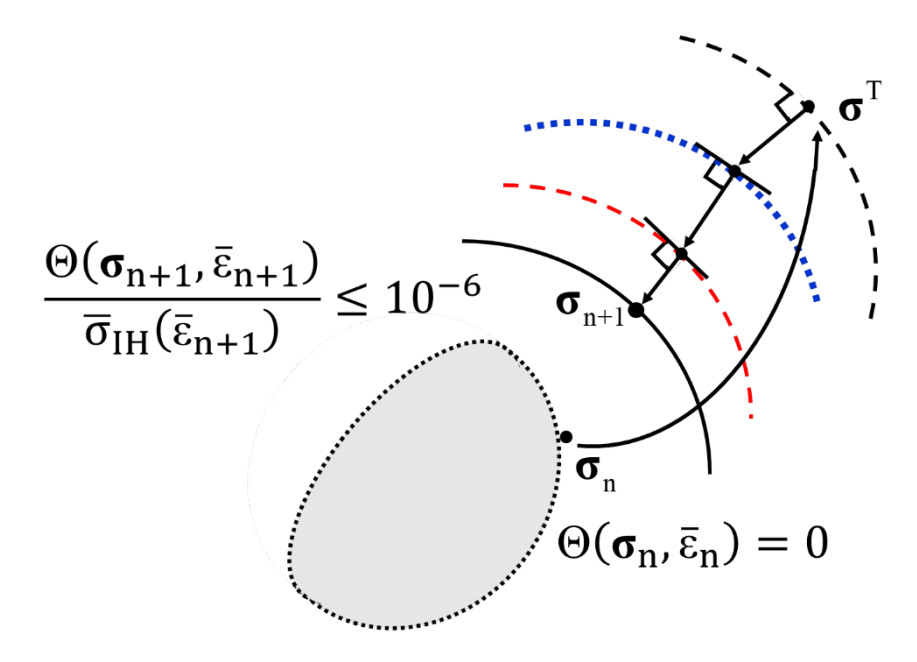


Figure 3: Schematic of the cutting-plane algorithm.

To maintain an approximately quadratic convergence rate in the implicit FE system globally, the continuum tangent modulus  $C^{ep}$  should be characterized as follows:

$$d\Theta = d\Phi(\mathbf{\sigma}) - d\bar{\sigma}_{IH}(\bar{\epsilon}) = \frac{\partial \Phi}{\partial \mathbf{\sigma}} d\mathbf{\sigma} - H'd\bar{\epsilon} = 0, \qquad (44)$$

$$d\mathbf{\sigma} = \mathbf{C}^{\mathrm{e}} : \left( d\mathbf{\varepsilon} - d\bar{\mathbf{\varepsilon}} \frac{\partial \Phi}{\partial \mathbf{\sigma}} \right), \tag{45}$$

$$d\mathbf{\sigma} = \left(\mathbf{C}^{e} - \frac{\mathbf{C}^{e} : \frac{\partial \Phi}{\partial \mathbf{\sigma}} \otimes \mathbf{C}^{e} : \frac{\partial \Phi}{\partial \mathbf{\sigma}}}{\frac{\partial \Phi}{\partial \mathbf{\sigma}} : \mathbf{C}^{e} : \frac{\partial \Phi}{\partial \mathbf{\sigma}} + \mathbf{H}'}\right) d\mathbf{\varepsilon} = \mathbf{C}^{ep} d\mathbf{\varepsilon}, \tag{46}$$

where the symbols of "\omega" represents the open product of two second-order tensors, defined as

$$\mathbf{A} \otimes \mathbf{B} = (a_{ij} \mathbf{e}_{i} \otimes \mathbf{e}_{i}) \otimes (b_{kl} \mathbf{e}_{k} \otimes \mathbf{e}_{l}) = a_{ij} b_{kl} \mathbf{e}_{i} \otimes \mathbf{e}_{i} \otimes \mathbf{e}_{k} \otimes \mathbf{e}_{l}. \tag{47}$$

As shown in Eq. (46), the first derivative of the plastic yielding function is necessary to obtain the continuum tangent operator throughout the stress integration procedure. With respect to the computation time, the analytical closed-form equation produces the best performance. However, extremely hard efforts are required to obtain the gradients of the plastic yielding

function as the material models become complicated to reproduce the material response under complex loading conditions. As an alternative, the numerical computation of the tangent operator, material-independent and less computation time, has been proposed and could be found in the literatures (Miehe, 1996; Pérez-Foguet et al., 2000; Seifert et al., 2007).

Note that the meaning of a tangent modulus/operator in a view of the computational approach is found in Appendix A.

### 3.3. Variational update form of anisotropic distortional hardening law

As reported in previous studies (Choi and Yoon, 2019; J. Lee et al., 2020; Yoon et al., 2020), the shape of the distorted yield surface for the distortional hardening model changes rapidly with the strain-path change. Thus, we focus on the variational form of the state variables relevant to the yield surface distortion with respect to the equivalent plastic strain. Because the state variables in the distortional hardening model in Eq. (1) are formulated as a function of the equivalent plastic strain, a strict variational rule should be applied in Eq. (32). Thus, main difference of the newly proposed algorithm introduced in this section is the dependence on the equivalent plastic strain and the other state variables defined in the distortional hardening model. The linearization of the consistency condition is carried out as follows:

$$\frac{\partial \Theta_{n+1} \left( \Delta \bar{\varepsilon}_{n+1}^{k} \right)}{\partial \Delta \bar{\varepsilon}} = -\frac{\partial \Phi_{n+1}^{k}}{\partial \sigma_{n+1}^{k}} : C^{e} : \frac{\partial \Phi_{n+1}^{k}}{\partial \sigma_{n+1}^{k}} + \frac{\partial \Phi_{n+1}^{k}}{\partial f_{1}^{(k)}} \frac{\partial f_{1}^{(k)}}{\partial \Delta \bar{\varepsilon}} + \frac{\partial \Phi_{n+1}^{k}}{\partial f_{2}^{(k)}} \frac{\partial f_{2}^{(k)}}{\partial \Delta \bar{\varepsilon}} + \frac{\partial \Phi_{n+1}^{k}}{\partial \hat{\mathbf{h}}^{s^{(k)}}} \frac{\partial \hat{\mathbf{h}}^{s^{(k)}}}{\partial \Delta \bar{\varepsilon}} - H'(\Delta \bar{\varepsilon}_{n+1}^{k}),$$
(48)

$$\delta(\Delta\gamma) = \delta(\Delta\bar{\epsilon})$$

$$= \frac{\Theta_{n+1}(\Delta \bar{\epsilon}_{n+1}^{k})}{\left(\frac{\partial \Phi_{n+1}^{k}}{\partial \boldsymbol{\sigma}_{n+1}^{k}} : \mathbf{C}^{e} : \frac{\partial \Phi_{n+1}^{k}}{\partial \boldsymbol{\sigma}_{n+1}^{k}} - \frac{\partial \Phi_{n+1}^{k}}{\partial f_{1}^{(k)}} \frac{\partial f_{1}^{(k)}}{\partial \Delta \bar{\epsilon}} - \frac{\partial \Phi_{n+1}^{k}}{\partial f_{2}^{(k)}} \frac{\partial f_{2}^{(k)}}{\partial \Delta \bar{\epsilon}} - \frac{\partial \Phi_{n+1}^{k}}{\partial \hat{\mathbf{h}}^{s^{(k)}}} \frac{\partial \hat{\mathbf{h}}^{s^{(k)}}}{\partial \Delta \bar{\epsilon}} + H'(\Delta \bar{\epsilon}_{n+1}^{k})\right)}, \quad (49)$$

where,

$$\frac{\partial \Phi}{\partial f_{1,2}} = \Phi^{(1-q)} f_{1,2}^{(q-1)} \left| 2\hat{\mathbf{h}}^s \mathbf{s} \right|^q \tag{50}$$

$$\frac{\partial f_{1,2}}{\partial \Delta \bar{\varepsilon}} = \frac{\partial f_{1,2}}{\partial g_{1,2}} \frac{\partial g_{1,2}}{\partial \Delta \bar{\varepsilon}} = f_{1,2}^{(q-1)} \left( -\frac{1}{g_{1,2}^{(q+1)}} \right) \frac{\partial g_{1,2}}{\partial \Delta \bar{\varepsilon}}$$
(51)

$$\frac{\partial \Phi}{\partial \hat{\mathbf{h}}^{\mathbf{s}}} = \Phi^{(1-q)} f_{1,2}^{\ q} (-1)^{1,2} \cdot 2 \cdot \left| 2 \hat{\mathbf{h}}^{\mathbf{s}} \mathbf{s} \right|^{(q-1)} \mathbf{s}. \tag{52}$$

The newly updated stress and equivalent plastic strain are given by Eq. (33) at the  $(k+1)^{th}$  iteration, and the relevant state variables are updated using Eqs. (3)–(16). The same termination condition in Eq. (43) as that of the previous cutting plane algorithm is used.

The continuum tangent modulus as a function of the all-evolutionary state variables is derived from the rate form of the consistency condition using Eq. (49) as follows:

$$\begin{split} \mathrm{d}\Theta &= \mathrm{d}\Phi \left( \mathbf{\sigma}, f_1, f_2, \, \hat{\mathbf{h}}^{\mathrm{s}} \right) - \mathrm{d}\bar{\sigma}_{\mathrm{IH}}(\bar{\epsilon}) = \frac{\partial \Phi}{\partial \mathbf{\sigma}} \mathrm{d}\mathbf{\sigma} + \frac{\partial \Phi}{\partial f_1} \mathrm{d}f_1 + \frac{\partial \Phi}{\partial f_2} \mathrm{d}f_2 + \frac{\partial \Phi}{\partial \hat{\mathbf{h}}^{\mathrm{s}}} \mathrm{d}\hat{\mathbf{h}}^{\mathrm{s}} - \mathrm{H'd}\bar{\epsilon} \\ &= \frac{\partial \Phi}{\partial \mathbf{\sigma}} \mathrm{d}\mathbf{\sigma} + \left( \frac{\partial \Phi}{\partial f_1} \frac{\partial f_1}{\partial \bar{\epsilon}} + \frac{\partial \Phi}{\partial f_2} \frac{\partial f_2}{\partial \bar{\epsilon}} + \frac{\partial \Phi}{\partial \hat{\mathbf{h}}^{\mathrm{s}}} \frac{\partial \hat{\mathbf{h}}^{\mathrm{s}}}{\partial \bar{\epsilon}} \right) \mathrm{d}\bar{\epsilon} - \mathrm{H'd}\bar{\epsilon} = 0 \;, \end{split} \tag{53}$$

$$\frac{\mathrm{d}\mathbf{\sigma}}{\mathrm{d}\mathbf{\epsilon}} = \mathbf{C}^{\mathrm{ep}} = \mathbf{C}^{\mathrm{e}} - \frac{\mathbf{C}^{\mathrm{e}} \frac{\partial \Phi}{\partial \mathbf{\sigma}} \otimes \mathbf{C}^{\mathrm{e}} \frac{\partial \Phi}{\partial \mathbf{\sigma}}}{\left(\frac{\partial \Phi}{\partial \mathbf{\sigma}} : \mathbf{C}^{\mathrm{e}} : \frac{\partial \Phi}{\partial \mathbf{\sigma}} - \frac{\partial \Phi}{\partial f_{1}} \frac{\partial f_{1}}{\partial \overline{\epsilon}} - \frac{\partial \Phi}{\partial f_{2}} \frac{\partial f_{2}}{\partial \overline{\epsilon}} - \frac{\partial \Phi}{\partial \hat{\mathbf{h}}^{\mathrm{s}}} \frac{\partial \hat{\mathbf{h}}^{\mathrm{s}}}{\partial \overline{\epsilon}} + \mathrm{H'}\right)},$$
(54)

where the rate forms of  $\frac{\partial f_1}{\partial \bar{\epsilon}}$ ,  $\frac{\partial f_2}{\partial \bar{\epsilon}}$ ,  $\frac{\partial h^s}{\partial \bar{\epsilon}}$  are computed as below.

$$\frac{\partial f_i}{\partial \bar{\varepsilon}} = \frac{\partial f_i}{\partial g_i} \frac{\partial g_i}{\partial \bar{\varepsilon}} \bigg|^{(k+1)} = f_i^{(q-1)} \left( -\frac{1}{g_i^{(q+1)}} \right) \frac{\partial g_i}{\partial \bar{\varepsilon}} \bigg|^{(k+1)} \quad \text{for } i = 1, 2$$
 (55)

$$\frac{d\hat{\mathbf{h}}^{s}}{d\bar{\varepsilon}} = k \cdot \operatorname{sgn}(\cos \chi) \left[ \left| \cos \chi \right|^{1/z} + g_{R} \right] \left( \hat{\mathbf{s}} - \cos \chi \, \hat{\mathbf{h}}^{s} \right) \right|^{(k+1)}$$
(56)

All the values are calculated at the  $(k+1)^{th}$  iteration, where the converged solutions are obtained.

Note that the GCPM considering the all-evolutionary plastic state variables presented in this section is called as "GCPM-N," and the aforementioned GCPM is named as "GCPM-O". And the whole process of the stress-update procedure is summarized in Appendix B.

#### 4. Numerical validation

Two stress-update algorithms based on the GCPM, that is, GCPM-O and GCPM-N, were integrated with the HAH-DPS model. The proposed numerical algorithms were implemented in the commercial FE software ABAQUS/Standard (Abaqus, 2018) via a user-defined material subroutine (UMAT). Two simulations subjected to different strain-path changes were conducted to evaluate the tangent operator with the all-evolutionary plastic state variables of the HAH-DPS model, that is, GCPM-N, for a global solution of an implicit FE code, and to demonstrate the convergence loss when the previously derived continuum tangent operator, that is, GCPM-O, is used. Note that the two cases led to the complex material behaviors such as the latent hardening and DPS effects, resulted in sudden shape change of the yield locus during plastic deformation. More in-depth study for the two cases regarding the numerical efficiency are presented in the following sections.

## 4.1. Combined plane-strain tension and simple shear loading of a notched specimen

A 1.2 mm-thick sheet metal specimen subjected to plane-strain tension followed by simple shear deformations was modeled with shell elements of four-node reduced integration (S4R). The number of elements and average mesh size were 2174 and 0.7 mm  $\times$  0.7 mm, respectively. Figure 4 describes the geometry of the specimen with dimension and displacement boundary condition for loading: (1) The upper part of the sample was fixed, and the lower part was moved down by 0.7 mm (plane-strain tension in the gauge section). (2) The load was then released (unloading). (3) Finally, the lower part was fixed, and the upper part was displaced by 3.5 mm in the horizontal direction (simple shear). The new tests were developed to reproduce the continuous or discontinuous strain path change by van Riel and van den Boogaard (2007), and the corresponding simulations were conducted by Ha et al. (2014). The loading path change indicators, cos χ and cos ω, defined in Eqs. (9) and (11) become zero during the prescribed strain-path change, and this loading path change is called the cross-loading condition. For the simulations during the second loading, the initial displacement increment  $\Delta u_{1, \text{ini.}} = 0.0035 \text{ mm}$ and maximum  $\Delta u_{1, \text{max.}} = 0.035$  mm were prescribed, and 1 s simulation time was subjected. The material coefficients of the EDDQ steel sample for the constitutive models were obtained from the authors' previous work (Lee et al., 2020), as listed in Table 1. The anisotropic material

properties were predicted by Yld2000-2d (Barlat et al., 2003), and the formulations are summarized in Appendix C. Note that the EDDQ steel sample exhibits stress overshooting or cross-hardening behavior under cross-loading conditions (Ha et al., 2013).

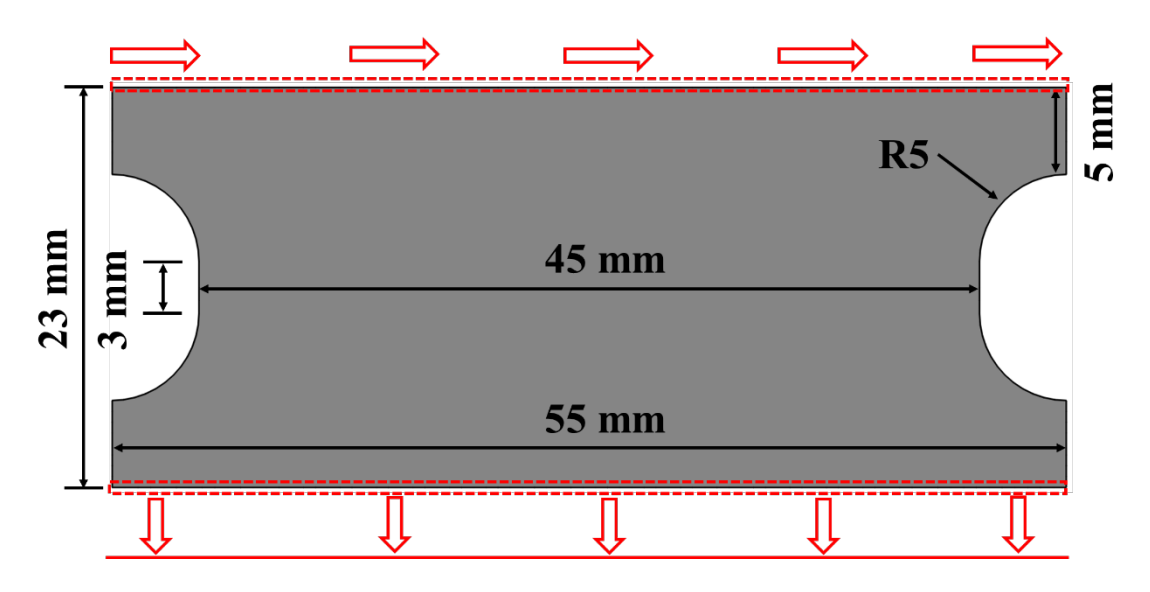


Figure 4: Specimen geometry subjected to plane-strain tension followed by simple shear

Table 1: Coefficients of the material models

Elastic properties and Swift hardening law									
Young's modulus (GPa)		Poisson's ratio		C (MPa)		ε <sub>0</sub>		N	
193.0		0.33		538.0		0.007	75	0.267	
Plastic anisotropy parameters for Yld2000-2d with exponent m = 6									
$\alpha_1$	$\alpha_2$		$\alpha_3$	α4	$\alpha_5$	$\alpha_6$	α7	$\alpha_8$	
1.014	1.118	8 0.931		0.892	0.904	0.811	1.029	0.918	
Distortional hardening parameters for HAH-DPS model with q = 2									
k	$k_1$	$k_2$	k <sub>3</sub>	k <sub>4</sub>	k <sub>5</sub>	L	k <sub>L</sub> S	ks	

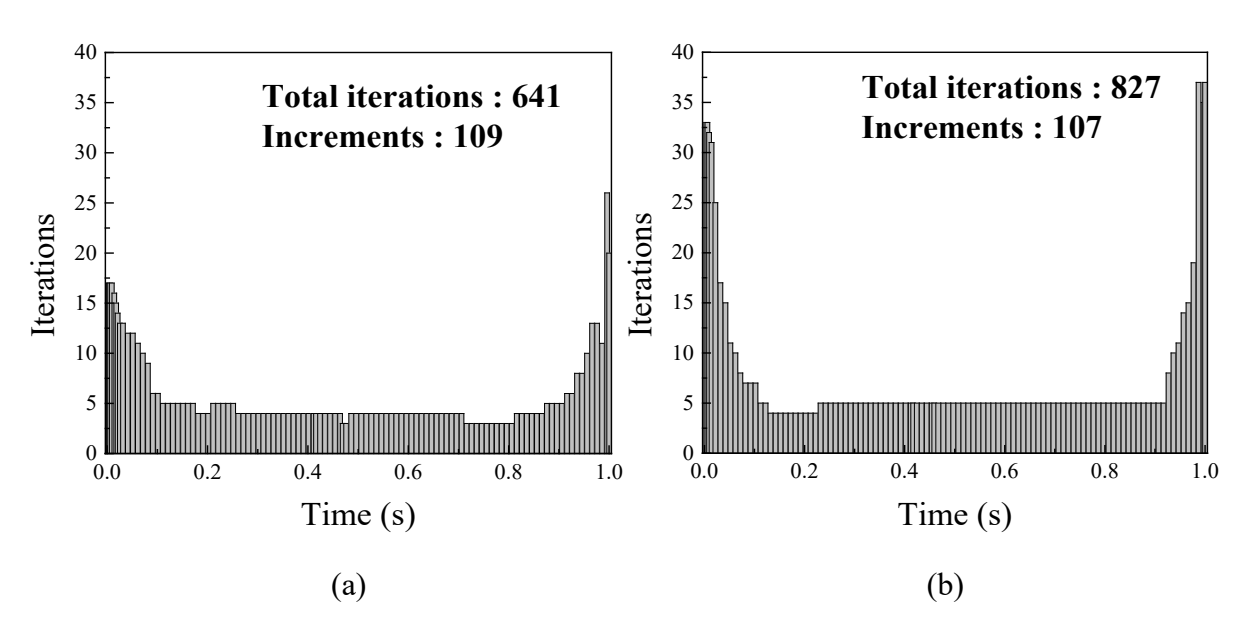


Figure 5: Maximum iterations for convergence in the stress integrating procedure during the second loading for (a) GCPM-N and (b) GCPM-O.

Figure 5 shows a comparison of the convergence behavior of the stress integration during the second loading between GCPM-N and GCPM-O. The total number of time-increments as well as the increment size were similar for both methods. The maximum number of iterations for convergence was also similar for most time increments, but a more iterative procedure was necessary for GCPM-O than for GCPM-N in the early stage of the loading path change, that is,  $\sim t < 0.05$  s. Nevertheless, both algorithms required several iterations at the beginning of the strain-path change, wherein the prior loading history was effective for the plastic deformation, owing to the overshooting flow behavior under cross-loading conditions, as shown in Figure 6 (a). To reproduce the cross-loading effect in the HAH-DPS model, the distorted yield locus rapidly expanded along the subsequent loading direction, as shown in Figure 6 (b). This was accompanied by drastic changes in the state variables of the model, which results in more iterative work to find the new stress update at the subsequent plastic deformation after strain-path change. For comparison, the yield locus of the isotropic hardening (IH) law was also plotted in Figure 6 (b) in the dotted black line. Note that the proposed distortional hardening

model follows the isotropic hardening behavior during the first loading, and because there was no prior loading history, both algorithms resulted in the same convergence behavior, which is not further examined in this study.

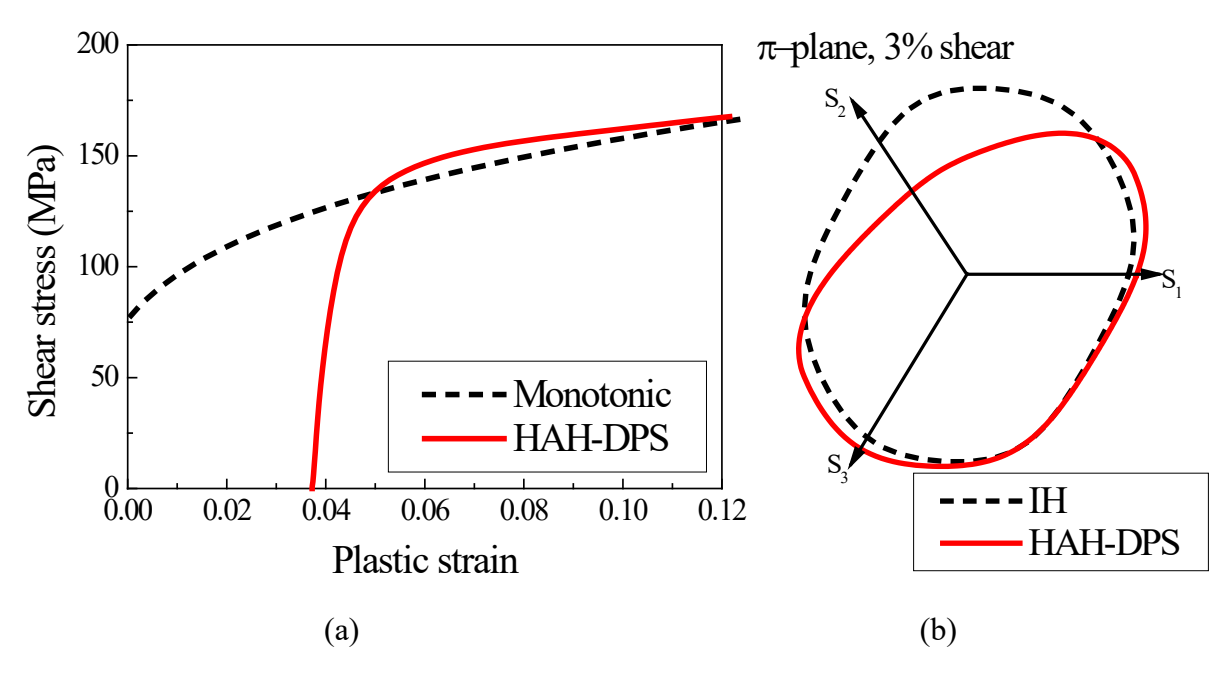
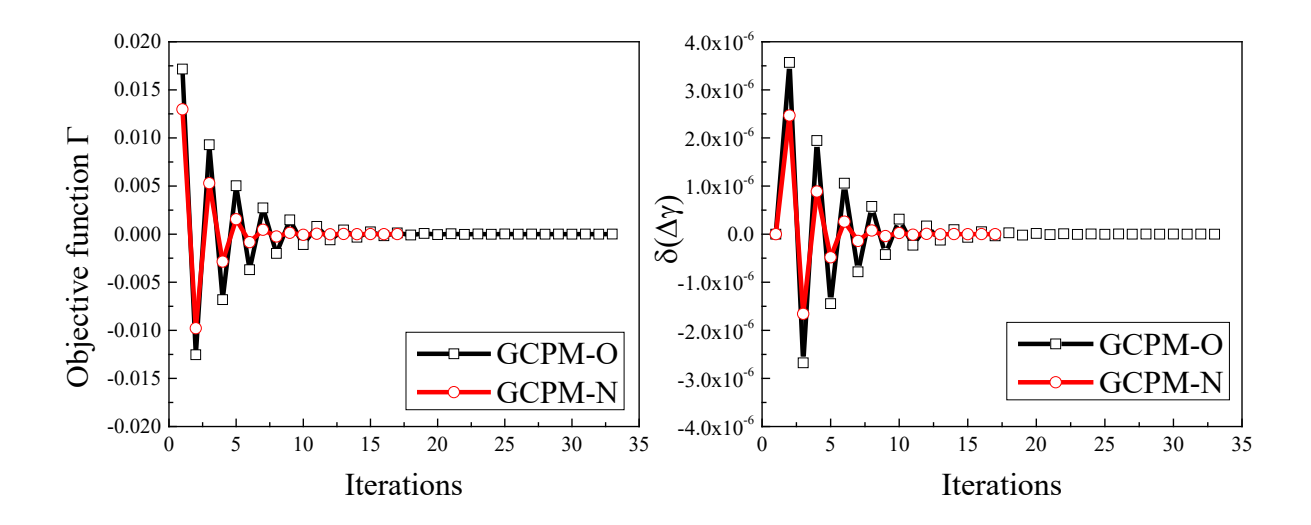


Figure 6: (a) Simple shear stress—plastic strain relationship and (b) the yield loci in the  $\pi$ -plane predicted by HAH-DPS and isotropic hardening (IH) models for the plane-strain tension followed by simple shear loading.



(a) (b)

Figure 7: Comparison between CGPM-N and GCPM-O during stress update in terms of (a) objective function  $\Gamma$ , and (b) the plastic multiplier increment  $\delta(\Delta \gamma)$ .

More detailed analyses on the iterative behavior of two stress integration algorithms are described in Figure 7 (a) and (b). Figure 7 (a) represents the evolution of the objective function  $\Gamma$ , as defined in Eq. (43), which should be less than a specified tolerance when the solution converges. It shows drastic changes in the objective function  $\Gamma$  in the initial stage of the iteration, corresponding to the loading path change, and as a result, it needs more iterative works owing to the severe distortion and sudden expansion of the yield surface. GCPM-O has more oscillated patterns in the objective function  $\Gamma$ , while GCPM-N can find a converged solution rapidly after 17 iterations. Figure 7 (b) shows the evolution of the plastic multiplier increment  $\delta(\Delta\gamma)$ , defined in Eqs. (32) and (49) for two different algorithms. During iterations, CGPM-N has smaller plastic multiplier increment changes than GCPM-O, which can accelerate the numerical convergence speed.

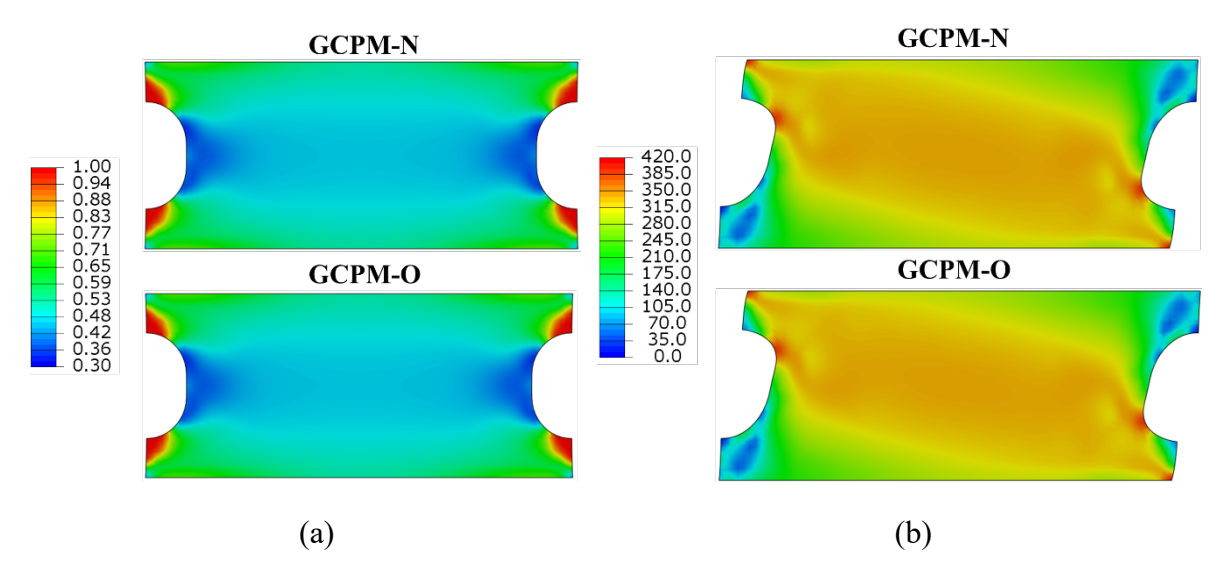


Figure 8: Comparison of FE results for (a) state variable  $g_1$  contours at the initial stage of the strain-path change, and (b) von-Mises stress distribution (Unit: MPa) at the final stage.

Figure 8 (a) shows the state variable  $g_1$  contours, representing Bauschinger effect, at the initial stage of the strain-path change. Almost same contours on the state variable  $g_1$  are observed in two different numerical schemes although  $g_1$  evolves with respect to the plastic multiplier as shown in Figure 7. And the corresponding quantitative analysis is carried out to calculate the least square error ( $\delta$ ) between two FE results as follows:

$$\delta := \sqrt{\frac{\sum_{i=1}^{i=N} \left(F_i^{\text{GCPM-N}} - F_i^{\text{GCPM-O}}\right)^2}{N}},$$
(57)

where N is the total number of elements, and F represents the FE result value.

Table 2: Least square errors between two different stress-update algorithms for Figure 8

State variable <i>g</i> <sub>1</sub>	von-Mises stress (MPa)	Stress in x- direction $\sigma_{xx}$ (MPa)	Stress in y- direction $\sigma_{yy}$ (MPa)	Shear stress $\tau_{xy}$ (MPa)	
2.8×10 <sup>-4</sup>	4.2	5.7	4.8	3.0	

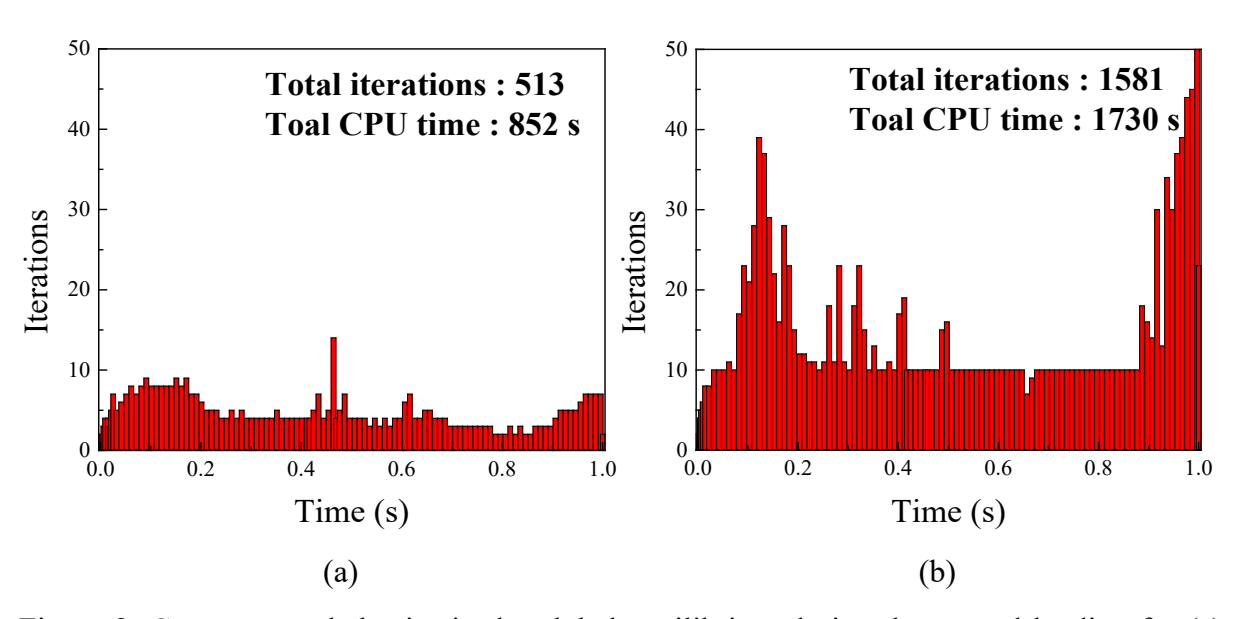


Figure 9: Convergence behavior in the global equilibrium during the second loading for (a) GCPM-N and (b) GCPM-O.

The least square error of the state variable  $g_1$  is provided in Table 2, quantitively. The result confirmed that almost same physical values are reproduced using the two different algorithms. Furthermore, the results in Figure 8 (b) show similar von-Mises stress distributions of two different stress-update algorithms at the final stage although each algorithm has different iteration histories as seen in Figure 5, and the corresponding errors are also shown in Table 2

Figure 9 shows the comparison of convergence results in a global equilibrium using GCPM-N and GCPM-O during the second loading. The graphs represent the number of iterations required to obtain a global equilibrium for each increment. As shown in the figure, GCPM-N leads to efficient and fast convergence results, and the total number of iterations of GCPM-N requires less than one-third of GCPM-O. Moreover, the total CPU time GCPM-N is much less than that of GCPM-O (852 s for the simulation using GCPM-N versus 1730 s for the simulation using GCPM-O). This demonstrates that GCPN-N, with an all-evolutionary state variable, is a more efficient and powerful approach in terms of convergence behavior in the global equilibrium.

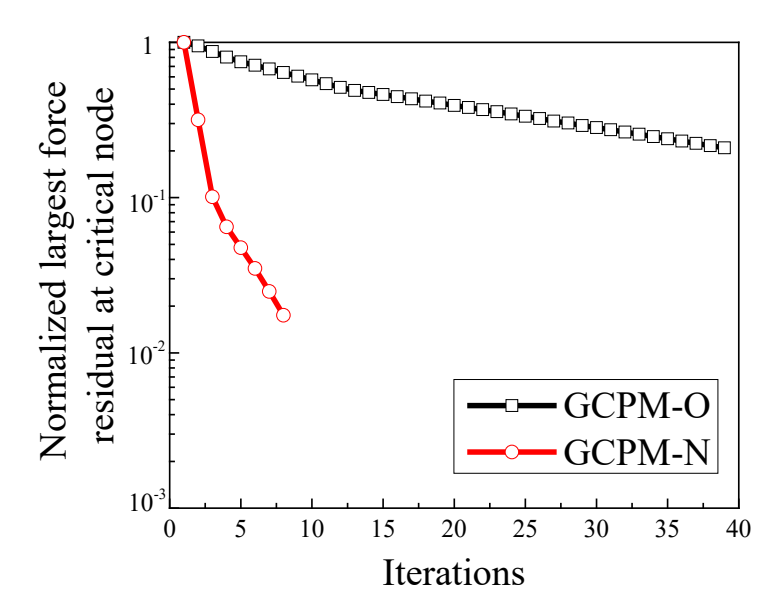


Figure 10: Comparison of normalized largest force residuals between GCPM-N and GCPM-O at a critical node during global iterations at a simulation time of 0.122 s.

The largest force residuals at the critical node are monitored during global iterations at the early stage of the strain-path change (at the simulation time of 0.122 s). The normalized largest force residuals, i.e., the largest force residuals divided by their initial residuals, are plotted in Figure 10. In the case of GCPM-O, the global solution converges after 40 iterations, whereas GCPM-N requires less than 10 iterations for the global convergence. The force residuals decrease rapidly for GCPM-N, and thus the convergence rate is much faster for GCPM-N than GCPM-O, as expected.

Figure 11 shows the convergence results in a global equilibrium when a large displacement increment is applied. In the simulations during the second loading, the initial and maximum displacement increments were prescribed as  $\Delta u_{1, \text{ ini.}} = 0.0035 \text{ mm}$  and  $\Delta u_{1, \text{ max.}} = 0.1 \text{ mm}$ , respectively. As shown in the figure, the maximum number of iterations required for GCPM-N is 80, whereas it is almost double for GCPM-O. This proves the efficiency and robustness of the proposed approach (GCPM-N) for a large displacement increment, equivalent to a large time increment, from the consideration of all-evolutionary state variables for the tangent operator and plastic multiplier increment.

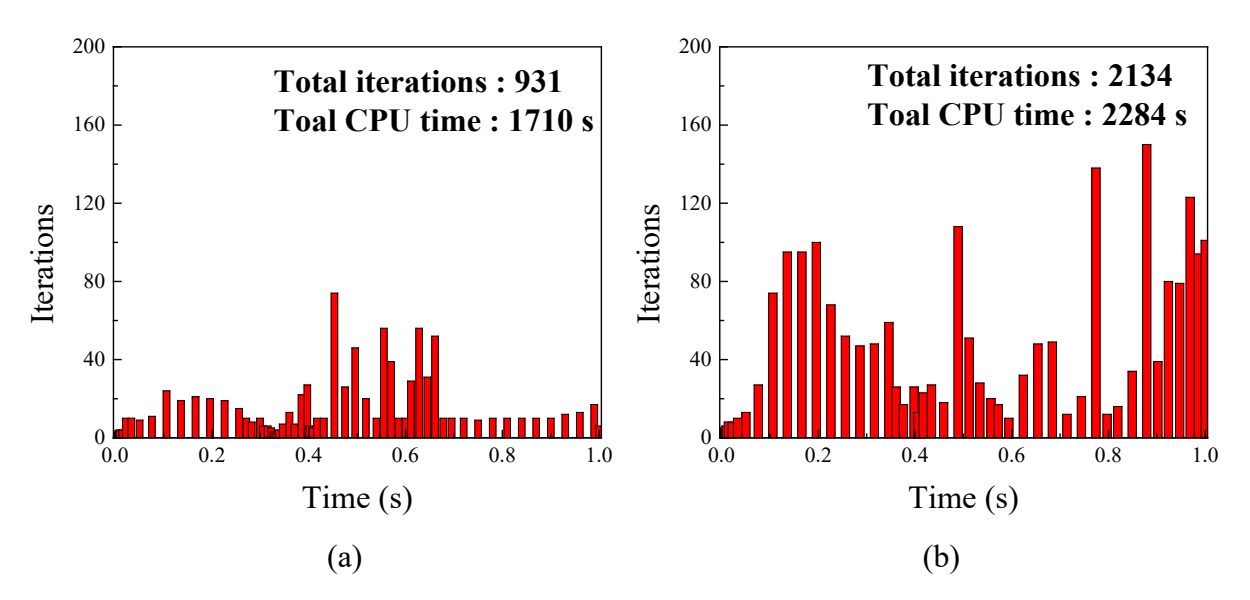


Figure 11: Convergence behavior in the global equilibrium during the second loading for (a) GCPM-N and (b) GCPM-O when the large displacement increment is prescribed.

# 4.2. Forming process problem: V-bending forming and springback

To show the numerical efficiency of the proposed numerical algorithm for the advanced distortional hardening law, a more demanding simulation was performed. A 0.1 mm-thick ferritic-stainless steel sheet was subjected to uniaxial tension at approximately 9% strain along the rolling direction (RD), and then the V-bending forming and springback simulations were conducted for a pre-strain sheet cut along 45 ° of the RD. All the FE simulations were conducted with implicit code using ABAQUS/Standard, and the influences of the stress integration algorithms on the convergence behavior of a global equilibrium solution were considered when complex problems such as contact issues between tools and sheet occur.

Figure 12 (a) shows the geometry and dimensions of the V-bending simulation. As shown in the figure, a punch radius of 1 mm was used, and the punch displacement along the vertical direction was 14.3 mm. According to the beam bending theory, a bending strain of 5 % on the outer surface of the sheet was subjected to the given punch displacement. The corresponding FE modeling for the components (die, punch, and blank) is shown in Figure 12 (b). Discrete rigid body element and 4-node shell element were used for the tools and sheet, respectively. Considering 2-fold symmetric property, only a quarter of the sheet sample was modeled with a sample size of 20 mm (length) × 5 mm (width). More than five elements were modeled for the corners of the tools. A Coulomb friction model with a constant friction coefficient of 0.15 was assumed for all contact surface interactions. Instead of uniaxial tension simulation for the first loading, a user-subroutine to define the initial solution-dependent state variable fields (SDVINI) was used. All the state variables related to the plasticity were obtained from a full-field tension simulation. For the second loading, which is the V-bending forming process for 1 s simulation time, the initial and maximum punch displacement increments were prescribed as  $\Delta u_{ini.} = 0.002$ mm and  $\Delta u_{max} = 0.2$  mm, respectively. The material parameters of the constitutive models for ferritic stainless steel are summarized in Table 3. Isotropic plastic yielding, that is, von-Mises criteria, was assumed in this study. The distortional hardening model was used to take into account of the fact that this steel sample also shows stress overshooting or cross-hardening behavior when the first and second loading directions are at 45 ° to each other (Bong et al., 2019). More details are provided in (J. Lee et al., 2020).

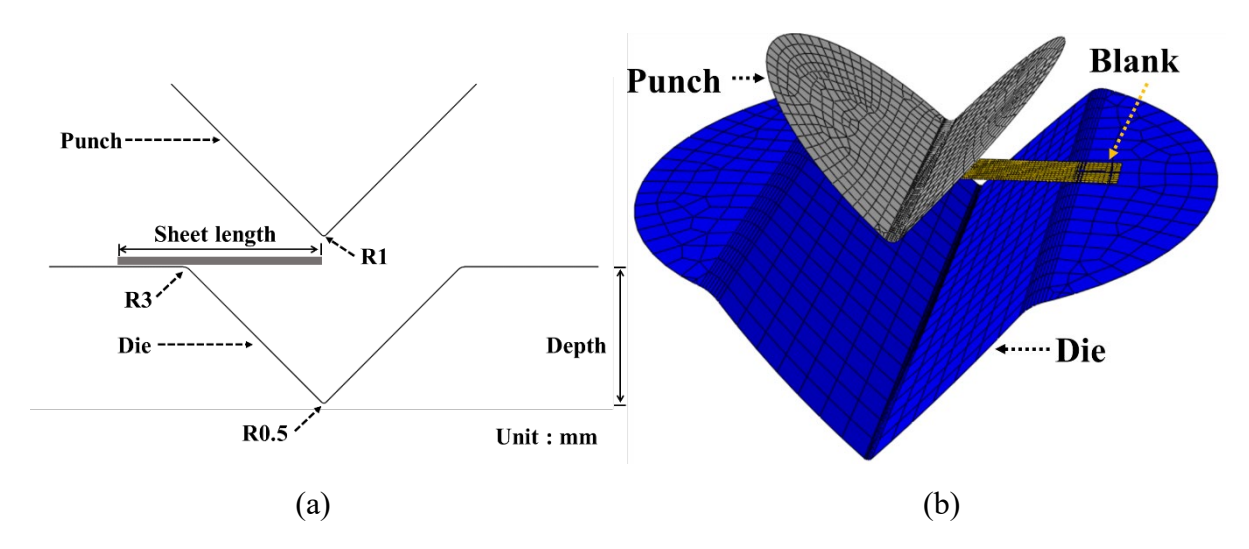


Figure 12: (a) Schematic of the V-bending tools and blank and (b) the corresponding FE model.

Table 3: The coefficients of the material models (J. Lee et al., 2020)

Elastic properties and Swift hardening law										
Young's modulus (GPa)		Poisson	's ratio	C (N	MPa)	{	ε <sub>0</sub>		n	
223.9		0.3	33	88	2.6	0.0056		0.224		
Plastic anisotropy parameters for Yld2000-2d with exponent m = 2										
$\alpha_1$	$\alpha_2$		$\alpha_3$	α4	$\alpha_5$	$\alpha_6$		$\alpha_7$	$\alpha_8$	
1.000	1.000	0 1.	000	1.000	1.000	1.000		1.000	1.000	
Distortional hardening parameters for HAH-DPS model with q = 2										
k	$\mathbf{k}_1$	$k_2$	$k_3$	k <sub>4</sub>	$k_5$	L	$k_{\rm L}$	S	$k_{\rm S}$	
18.7	580.0	10.0	0.9	0.88	24.0	1.65	384.0	1.0	0.0	

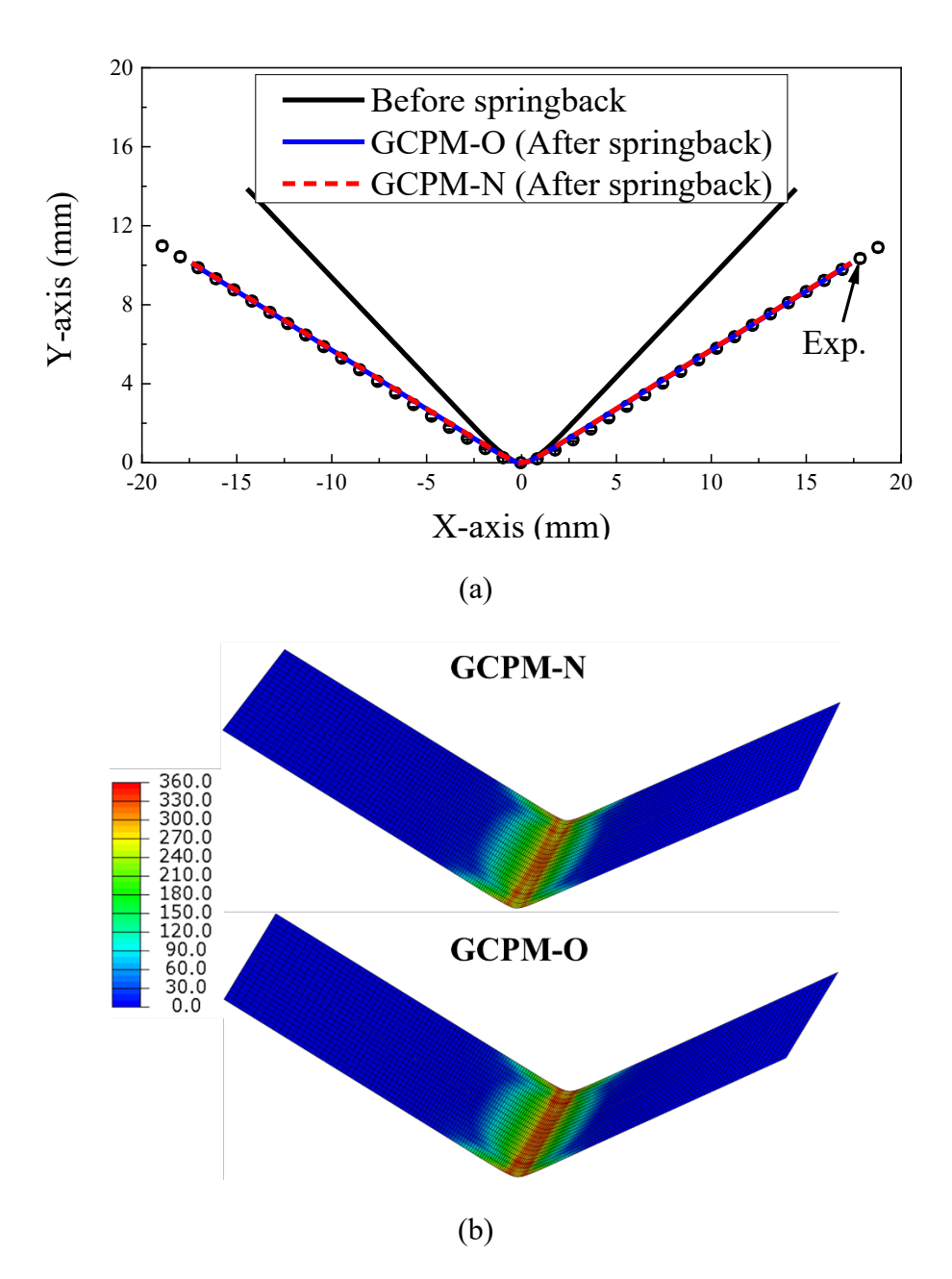


Figure 13: Comparison of springback results between GCPM-N and GCPM-O: (a) Profile and (b) residual stress (Unit: MPa). The experimental data refer to Lee et al. (J. Lee et al., 2020).

The springback results of the V-bending simulation with a pre-strained specimen are shown in Figure 13. The comparison shows that both stress-update algorithms predict almost identical springback profiles (Figure 13 (a)) and very similar residual stress distributions with negligible differences (Figure 13 (b)). During the forming simulations, the total number of iterations necessary to converge to the solution for a given strain increment locally were, 391 and 252

for GCPM-O and GCPM-N, respectively. Moreover, the average iterations per increment to converge, i.e., the total iteration divided by the number of increments, were 4.2 and 4.4 for GCPM-O and GCPM-N, respectively, showing similar local convergence speed for GCMP-O to that of GCPM-N. This is because GCPM-N requires a smaller number of increments during the forming process. Note that the two algorithms show the same convergence behavior during the springback simulation because of purely elastic deformation.

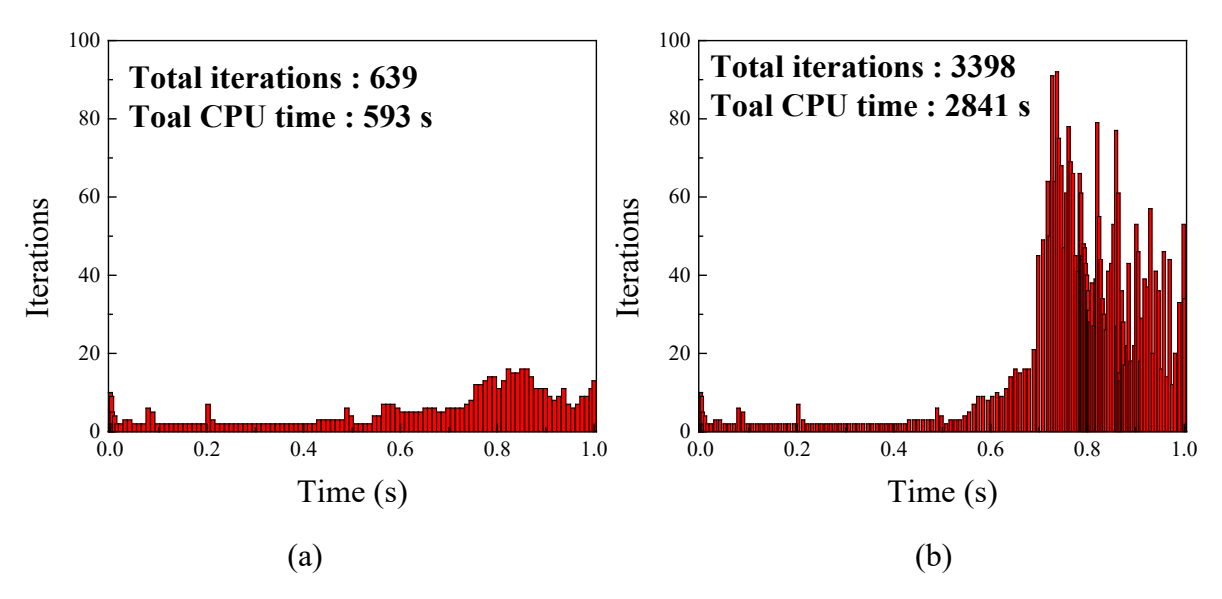


Figure 14: Convergence behavior in the global equilibrium during the V-bending forming process for (a) GCPM-N and (b) GCPM-O.

Figure 14 shows a comparison of the convergence results in the global equilibrium between the two different tangent operators during the forming process. Importantly, the convergence behavior of the global equilibrium exhibits much better efficiency in GCPM-N because of the smaller number of iterations and larger increments required than GCPM-O. As already pointed out, the poor convergence behavior of GCPM-O in a global equilibrium was observed, especially when the material experienced a cross-loading effect with latent hardening, even though a smaller increment was prescribed during the simulation. The number of iterations necessary to obtain a solution globally using GCPM-N was approximately one-fifth that of

GCPM-O. Moreover, the computation CPU time was reduced by over 70% for the proposed GCPM-N algorithm.

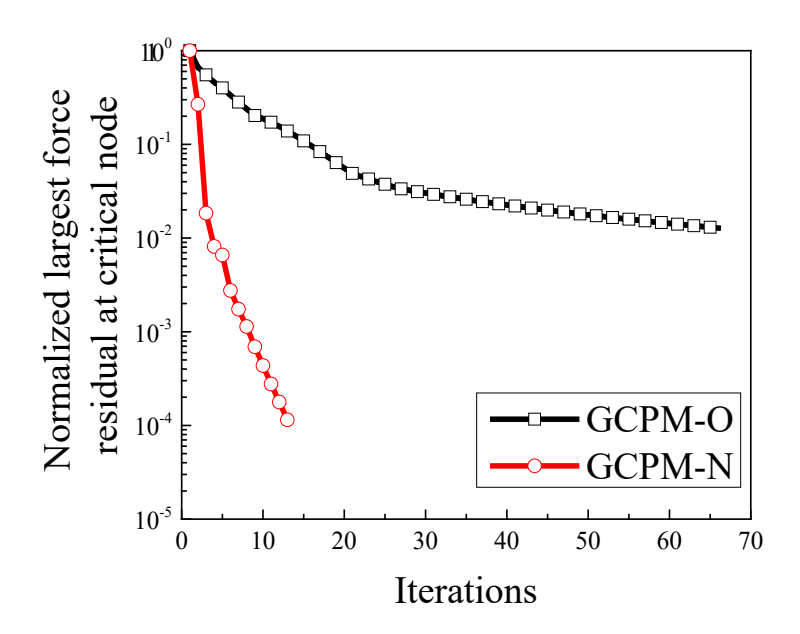


Figure 15: Comparison of normalized largest force residuals between GCPM-N and GCPM-O at critical node during global iterations at a simulation time of 0.775 s.

More in-depth analysis on the global convergence behavior is conducted. Figure 15 monitors the largest force residuals of the global iterations at a simulation time of 0.775 s during the V-bending forming process. The global solution is obtained for GCPM-O after 65 iterations, but it is only 15 iterations for GCPM-N. As a result of that, the convergence speed of GCPM-N is much faster than GCPM-O as analyzed in Figure 14, which is the same result with the plane-strain tension and simple shear of the notch specimen in Section 4.1.

Figure 16 shows the comparison of FE results between GCPM-O and GCPM-N at the simulation time of 0.775 s during V-bending forming process. The distribution of the state variable  $g_L$ , which captures the cross-hardening effect, is shown in Figure 16 (a). The FE simulations of two different algorithms lead to almost identical results, qualitatively. In addition, von-Mises stress contours are evaluated for two stress update algorithms in Figure 16 (b). The FE results reveal that both stress integration algorithms produce the similar stress distribution even with drastic yield surface changes upon strain-path changes, such as sudden expansion of

the yield surface due to the cross-hardening effect, but the convergence rate for both algorithms are totally different. Thus, in conclusion, the analysis indicates that GCPM-N has an advantage in the global convergence speed but requires the complex mathematical expression to implement. In contrast, the simple formulation of GCPM-O is of advantage to implement although relatively slow convergence speed.

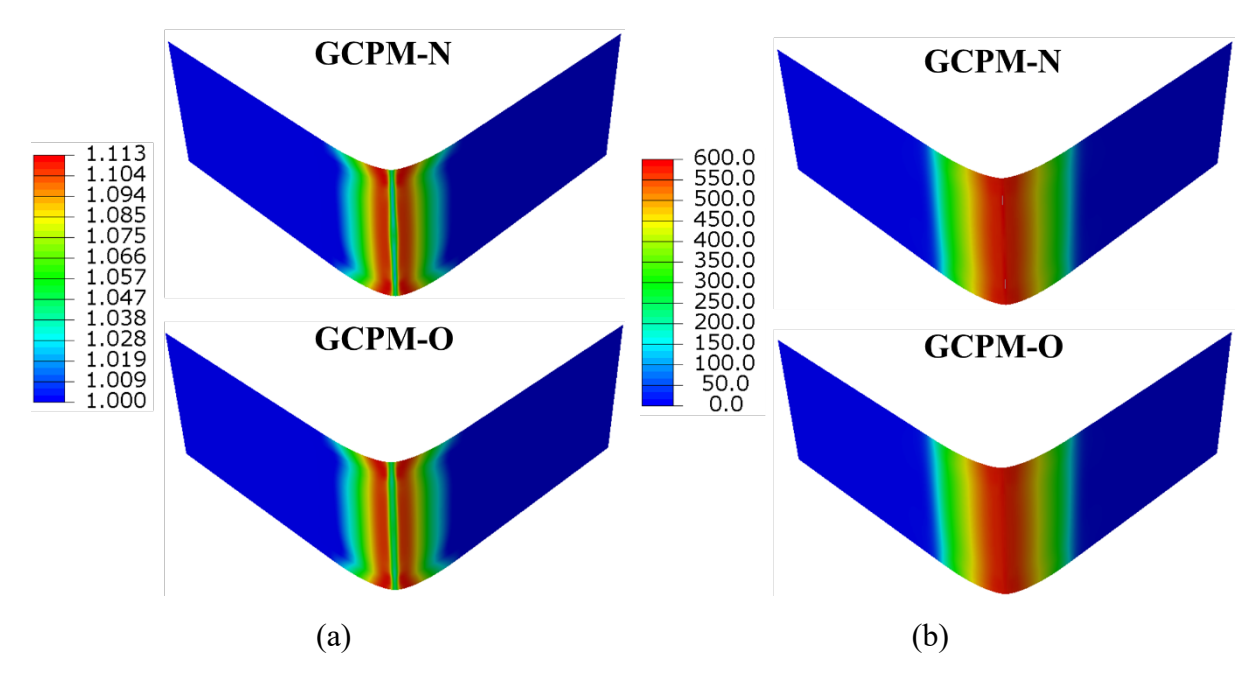


Figure 16: Comparison of FE results for (a) state variable  $g_L$  contour, and (b) von-Mises stress distribution (Unit: MPa) at a simulation time of 0.775 s during V-bending forming.

## 5. Summary and conclusions

In this study, a stress-update algorithm based on the GCPM method was reformulated for the HAH-DPS distortional hardening law, namely GCPM-N, and implemented in the commercial FE software ABAQUS/Standard via UMAT. The proposed numerical algorithm can capture anisotropic hardening behaviors such as the Bauschinger effect, transient hardening, differential permanent softening with respect to the loading direction, and cross-loading effect with latent hardening/contraction by introducing the concept of yield surface distortion. In particular, the plastic multiplier for obtaining the solution during stress integration and the continuum tangent operator for finding a solution in a global equilibrium were derived considering the all-evolutionary state variables. To compare the efficiency and robustness of the developed (GCPM-N) and previously proposed (GCPM-O) stress integration algorithms, two FE simulations were conducted: plane-strain tension followed by simple shear and V-bending forming simulations with a pre-strained specimen. The main findings of this study can be summarized as follows:

- From the cross-loading simulation result of the plane-strain tension followed by simple shear deformation, the developed numerical algorithm, GCPM-N, showed a similar iterative behavior for convergence, given a strain increment with that of the previous stress-update algorithm, GCPM-O, whereas GCPM-O required more iterations in the subsequent plastic deformation after strain-path change.
- In view of the global convergence behavior, GCPM-N required one-third of the iterations exhibited by GCPM-O, and half of the computation time consumed by GCPM-O, which showed better computational speed. When the time increment enhanced, the computational efficiency of the GCPM-N was preserved.
- From the forming and springback simulations of a complex geometrical problem, both
  algorithms resulted in the same springback predictions, and similar local convergence
  behavior was evaluated based on the average iterations. However, smaller time
  increments were required for GCPM-O.
- By comparing the iteration numbers for a global equilibrium, the proposed GCPM-N considering all-evolutionary plastic state variables was found to be computationally

faster and more efficient. However, although the previous numerical algorithm GCPM-O required more iterations in a global equilibrium resulting in the loss of the computational speed, GCPM-O still had the advantage of preserving the simple formulation from the implementation point of view, even for a complex constitutive model.

# Acknowledgment

J. Lee and H.J. Bong appreciate the supports by the Fundamental Research Program of the Korea Institute of Materials Science, South Korea (KIMS, PNK8440). J. Ha appreciates the support by the U.S. National Science Foundation and was accomplished under the Grant No. OIA-1757371.

### Appendix A. Tangent operator-Material stiffness tensor

In order to describe the role of a tangent operator (or called material stiffness tensor) developed in the preceding chapter, a typical numerical solution scheme for the elastoplastic implicit boundary value problem (IBVP) is explained in the context of the FE method.

Only considering the static problem case, the equilibrium equations derived from the virtual work equations are expressed symbolically as

$$\psi(\sigma_{n+1}) = \mathbf{F}^{\text{int}}(\sigma_{n+1}) - \mathbf{F}_{n+1}^{\text{ext}} = \mathbf{0},$$
(A.1)

where  $\mathbf{F}^{\text{int}}$  and  $\mathbf{F}^{\text{ext}}$  represent the discrete internal and external load vectors, respectively.

By applying the linearization method at the  $\underline{i}^{th}$  equilibrium iteration in Eq. (A.1), the following linear system of equations is obtained as

$$\left[\mathbf{F}^{\text{int}}\left(\mathbf{\sigma}_{n+1}^{(i)}\right) - \mathbf{F}_{n+1}^{\text{ext}}\right] + \mathbf{K}_{n+1}^{(i)} \Delta \mathbf{d}_{n+1}^{(i+1)} = \mathbf{0},\tag{A.2}$$

where  $\Delta \mathbf{d}_{n+1}^{(i+1)}$  is the incremental nodal displacement at the  $(i+1)^{\text{th}}$  iteration, and the global stiffness operator  $\mathbf{K}_{n+1}^{(i)}$  is defined as

$$\mathbf{K}_{n+1}^{(i)} = \frac{\partial \mathbf{\psi}}{\partial \mathbf{d}_{n+1}^{(i)}} = \frac{\partial \mathbf{F}^{\text{int}} \left( \mathbf{\sigma}_{n+1}^{(i)} \right)}{\partial \mathbf{d}_{n+1}^{(i)}} = \frac{\partial \mathbf{F}^{\text{int}} \left( \mathbf{\sigma}_{n+1}^{(i)} \right)}{\partial \mathbf{\sigma}_{n+1}^{(i)}} \frac{\partial \mathbf{\sigma}_{n+1}^{(i)}}{\partial \mathbf{\epsilon}_{n+1}^{(i)}} \frac{\partial \mathbf{\epsilon}_{n+1}^{(i)}}{\partial \mathbf{d}_{n+1}^{(i)}}. \tag{A.3}$$

This linear equation in Eq. (A.2) could be solved when the tangent operator  $\frac{\partial \sigma_{n+1}^{(i)}}{\partial \varepsilon_{n+1}^{(i)}}$  is provided.

As clearly seen in previous equation, the tangent operator derived from the stress integration algorithm affects a calculation of the global stiffness operator.

By solving the following equation, the new global discrete displacement field is obtained as

$$\Delta \mathbf{d}_{n+1}^{(i+1)} = -\left[\mathbf{K}_{n+1}^{(i)}\right]^{-1} \left[\mathbf{F}^{\text{int}}\left(\boldsymbol{\sigma}_{n+1}^{(i)}\right) - \mathbf{F}_{n+1}^{\text{ext}}\right]. \tag{A.4}$$

Note that the simulation results are not affected by the inaccurate definition of the tangent operator, while the convergence rate is.

Remark is that two types of material tangent operators can be selected to construct the structure stiffness operator: continuum tangent modulus and consistent tangent modulus (Gu et al., 2011; Simo and Taylor, 1985; Szabó and Jonas, 1995). The continuum tangent modulus is defined as the differentiation with respect to the infinitesimal strain increment d $\varepsilon$  of the rate constitutive equation d $\sigma$  while the consistent tangent modulus (also called algorithmic tangent modulus) is obtained through direct differentiation of the incremental constitutive equation  $\Delta \sigma$  with respect to the total incremental strain  $\Delta \varepsilon$ .

More rigorous expression of the tangent operator could be summarized as below.

The following relationship is considered.

$$\mathbf{\sigma} = \frac{\rho}{\rho_0} \mathbf{F} \mathbf{S} \mathbf{F}^{\mathrm{T}},\tag{A.5}$$

where  $\sigma$  and S are the Cauchy stress and  $2^{nd}$  Piola-Kirchhoff stress tensors, respectively. F is deformation gradient tensor,  $\rho$  and  $\rho_0$  are the final and initial densities of the material.

The relationship for the spatial gradient of the velocity ( $\mathbf{L} = \dot{\mathbf{F}}\mathbf{F}^{-1}$ ,  $\dot{\mathbf{F}} = \partial \mathbf{F}/\partial t$ ) results in

$$\dot{\mathbf{\sigma}} = \frac{\dot{\rho}}{\rho_0} \dot{\mathbf{\sigma}} + \mathbf{L} \mathbf{\sigma} + \frac{\rho}{\rho_0} \mathbf{F} \dot{\mathbf{S}} \mathbf{F}^{\mathrm{T}} + \mathbf{\sigma} \mathbf{L}^{\mathrm{T}}. \tag{A.6}$$

Two assumptions are applied, and the above equation becomes a simpler expression to conveniently obtain the material tangent operator: (1) small deformation condition ( $\mathbf{F} \cong \mathbf{I}$ ), (2) incompressibility condition ( $\dot{\rho} \cong 0$  and  $\rho = \rho_0$ ). And the following equation is obtained.

$$\dot{\sigma} = \mathbf{L}\boldsymbol{\sigma} + \dot{\mathbf{S}} + \boldsymbol{\sigma}\mathbf{L}^{\mathrm{T}} = \mathbf{D}\boldsymbol{\sigma} + \mathbf{W}\boldsymbol{\sigma} + \dot{\mathbf{S}} + \boldsymbol{\sigma}\mathbf{D} - \boldsymbol{\sigma}\mathbf{W}, \tag{A.7}$$

where **D** and **W** are the rate of the deformation tensor and the spin tensor, respectively. Note that these approximations were applied only to conveniently obtain the material stiffness tensor.

Using the formulation  $\dot{\boldsymbol{\sigma}} = \dot{\boldsymbol{\sigma}}^J + \mathbf{W}\boldsymbol{\sigma} - \boldsymbol{\sigma}\mathbf{W}$ , where  $\dot{\boldsymbol{\sigma}}^J$  is the Jaumann rate of the Cauchy stress, the expression Eq. (A.7) leads to

$$\dot{\mathbf{S}} = \dot{\mathbf{\sigma}}^{J} - \mathbf{\sigma} \mathbf{D} - \mathbf{D} \mathbf{\sigma}. \tag{A.8}$$

The approximations hold for  $d\mathbf{E} \cong \mathbf{D} dt$ , where  $\mathbf{E}$  is Green-Lagrange strain tensor, under the small deformation condition ( $\mathbf{F} \cong \mathbf{I}$ ), and it leads to

$$d\mathbf{S} = d\mathbf{\sigma}^{J} - \mathbf{\sigma}d\mathbf{\varepsilon} - d\mathbf{\varepsilon}\mathbf{\sigma} \tag{A.9}$$

where  $d\sigma^{J} = \mathbf{C}^{ep} d\mathbf{\epsilon}$ , and  $\mathbf{C}^{ep}$  is defined in this study.

More details are found in literatures (Waffenschmidt et al., 2014; Yoon et al., 1999b).

#### Appendix B. Summary of the stress-update algorithm for the HAH-DPS model

A step-by-step implementation of the stress-update algorithms for the HAH-DPS model discussed in the paper is summarized for convenience in Box B.1.

Box B.1. Algorithmic box for the HAH-DPS material model.

#### 1. Initialize

$$\begin{split} k &= 0, \ \ \boldsymbol{\sigma}_{n+1}^{(0)} = \boldsymbol{\sigma}^T = \boldsymbol{\sigma}_n + \boldsymbol{C}^e : \Delta \boldsymbol{\epsilon}_{n+1}, \overline{\boldsymbol{\epsilon}}_{n+1}^{(0)} = \overline{\boldsymbol{\epsilon}}_n, \ \ \Delta \boldsymbol{\gamma} = 0, \ \ \boldsymbol{g}_L^{(0)} = (\boldsymbol{g}_L)_n, \ \ \boldsymbol{g}_S^{(0)} = \\ (\boldsymbol{g}_S)_n, \ \boldsymbol{g}_R^{(0)} &= (\boldsymbol{g}_R)_n, \ \boldsymbol{g}_i^{(0)} = (\boldsymbol{g}_i)_n \ \ \text{for } i = 1-4, \text{ and } \ \boldsymbol{\hat{h}}_{n+1}^{S^{(0)}} = \boldsymbol{\hat{h}}_n^S. \end{split}$$

2. Check the consistency condition in Eq. (27)

IF: 
$$\Theta(\boldsymbol{\sigma}^T, \overline{\epsilon}_n) = \Phi(\boldsymbol{\sigma}^T) - \overline{\sigma}_{IH}(\overline{\epsilon}_n) \leq 0$$
, then terminate.

ELSE: Go to 3

3. Calculate the incremental plastic multiplier  $\delta(\Delta \gamma)$ 

IF: For GCPN-N algorithm, then compute  $\delta(\Delta \gamma)$  using Eq. (49)

$$\delta(\Delta \gamma) = \frac{\Theta_{n+1}(\Delta \bar{\epsilon}_{n+1}^{k})}{\left(\frac{\partial \Phi_{n+1}^{k}}{\partial \sigma_{n+1}^{k}} : C^{e} : \frac{\partial \Phi_{n+1}^{k}}{\partial \sigma_{n+1}^{k}} - \frac{\partial \Phi_{n+1}^{k} \partial J_{1}^{(k)}}{\partial J_{1}^{(k)}} - \frac{\partial \Phi_{n+1}^{k} \partial J_{2}^{(k)}}{\partial J_{2}^{(k)}} - \frac{\partial \Phi_{n+1}^{k} \partial h^{s}^{(k)}}{\partial h^{s}} - \frac{\partial \Phi_{n+1}^{k} \partial h^{s}^{(k)}}{\partial h^{s}} + H'(\Delta \bar{\epsilon}_{n+1}^{k})\right)}.$$

ELSE: Compute  $\delta(\Delta \gamma)$  for GCPN-O algorithm, using Eq. (32).

4. Obtain the equivalent plastic strain increments in Eq. (31)

$$\Delta \bar{\varepsilon}_{n+1}^{(k+1)} = \Delta \bar{\varepsilon}_{n+1}^{k} + \delta(\Delta \gamma).$$

5. Update the stress and equivalent strain in Eq. (33)

$$\boldsymbol{\sigma}_{n+1}^{(k+1)} = \boldsymbol{\sigma}_{n+1}^{(k)} + \delta(\Delta \overline{\epsilon}) \mathbf{C}^{e} : \frac{\partial \Phi_{n+1}^{k}}{\partial \boldsymbol{\sigma}_{n+1}^{k}},$$

$$\overline{\varepsilon}_{n+1}^{(k+1)} = \overline{\varepsilon}_{n+1}^{(k)} + \Delta \overline{\varepsilon}_{n+1}^{(0)}.$$

6. Update the state variables of the HAH-DPS model at  $(k+1)^{th}$  iteration through

7. Check the consistency condition in Eq. (28)

$$\Theta_{n+1}^{k+1} = \Phi\left(\boldsymbol{\sigma}_{n+1}^{(k+1)}\right) - \bar{\sigma}_{IH}\left(\bar{\epsilon}_{n+1}^{(k+1)}\right).$$

IF: 
$$\Gamma = \frac{\left|\Theta_{n+1}^{k+1}\right|}{\overline{\sigma}_{\text{IH}}\left(\overline{\varepsilon}_{n+1}^{(k+1)}\right)} < \text{Tol in Eq. (43), Go to 10.}$$

ELSE: Set  $k \leftarrow k+1$  and GO TO 3.

8. Computer the tangent operator  $\mathbf{C}^{ep}$ 

IF: For GCPN-N algorithm, then compute C<sup>ep</sup> using Eq. (54)

$$\mathbf{C}^{\mathrm{ep}} = \mathbf{C}^{\mathrm{e}} - \frac{\mathbf{C}^{\mathrm{e}\frac{\partial \Phi}{\partial \sigma}} \otimes \mathbf{C}^{\mathrm{e}\frac{\partial \Phi}{\partial \sigma}}}{\left(\frac{\partial \Phi}{\partial \sigma} : \mathbf{C}^{\mathrm{e}} : \frac{\partial \Phi}{\partial \sigma} - \frac{\partial \Phi}{\partial f_{1}} \frac{\partial f_{1}}{\partial f_{1}} \frac{\partial \Phi}{\partial \bar{f}_{2}} - \frac{\partial \Phi}{\partial f_{2}} \frac{\partial \hat{h}^{s}}{\partial \bar{f}^{s}} + \mathbf{H}'\right)}.$$

ELSE: Compute tangent operator for GCPN-O algorithm, using Eq. (45).

## Appendix C. Anisotropic non-quadratic yield function: Yld2000-2d

The equivalent stress of Yld2000-2d model (Barlat et al., 2003) is express as

$$\xi(\boldsymbol{\sigma}) = \left(\frac{\xi' + \xi''}{2}\right)^{\frac{1}{a}} = \bar{\sigma}_e, \qquad (B.1)$$

$$\xi' = \left| S_1^{(1)} - S_2^{(1)} \right|^a \text{ and } \xi'' = \left| 2S_2^{(2)} + S_1^{(2)} \right|^a + \left| 2S_1^{(2)} + S_2^{(2)} \right|^a, \tag{B.2}$$

where 'a' represents an exponent, recommended as 8 for FCC metals and 6 for BCC metals.  $\bar{\sigma}_e$  is the equivalent stress, and  $S_{1,2}^{(i)}$  (i=1,2) represent the principal stresses calculated from the following tensor  $S^{(i)}$  (i=1,2). Two linear transformations from the Cauchy stress  $\sigma$  to  $S^{(i)}$  (i=1,2) are used to reproduce the anisotropic property of metals, and defined as

$$\mathbf{S}^{(1,2)} = \mathbf{C}^{(1,2)} \cdot \mathbf{s} = \mathbf{C}^{(1,2)} \cdot \mathbf{T} \cdot \mathbf{\sigma} = \mathbf{L}^{(1,2)} \cdot \mathbf{\sigma}. \tag{B.3}$$

The tensor **T** has a role to transform the Cauchy stress  $\sigma$  to the deviatoric stress s via, and the tensors  $C^{(1)}$  and  $C^{(2)}$  include the anisotropic property of metals.  $L^{(1)}$  and  $L^{(2)}$  are the two linear transformations product and their matrix forms are expressed as follows:

$$\begin{bmatrix}
S_{xx}^{(i)} \\
S_{yy}^{(i)} \\
S_{xy}^{(i)}
\end{bmatrix} = \begin{bmatrix}
L_{11}^{(i)} & L_{12}^{(i)} & 0 \\
L_{21}^{(i)} & L_{22}^{(i)} & 0 \\
0 & 0 & L_{66}^{(i)}
\end{bmatrix} \begin{bmatrix}
\sigma_{xx} \\
\sigma_{yy} \\
\sigma_{xy}
\end{bmatrix} \text{ with } i = 1,2$$
(B.4)

$$\begin{bmatrix} L_{11}^{(1)} \\ L_{12}^{(1)} \\ L_{21}^{(1)} \\ L_{22}^{(1)} \\ L_{66}^{(1)} \end{bmatrix} = \begin{bmatrix} 2/3 & 0 & 0 \\ -1/3 & 0 & 0 \\ 0 & -1/3 & 0 \\ 0 & 2/3 & 0 \\ 0 & 0 & 1 \end{bmatrix} \begin{bmatrix} \alpha_1 \\ \alpha_2 \\ \alpha_7 \end{bmatrix} \text{ and } \begin{bmatrix} L_{11}^{(2)} \\ L_{12}^{(2)} \\ L_{21}^{(2)} \\ L_{22}^{(2)} \\ L_{66}^{(2)} \end{bmatrix} = \frac{1}{9} \begin{bmatrix} -2 & 2 & 8 & -2 & 0 \\ 1 & -4 & -4 & 4 & 0 \\ 4 & -4 & -4 & 1 & 0 \\ -2 & 8 & 2 & -2 & 0 \\ 0 & 0 & 0 & 0 & 9 \end{bmatrix} \begin{bmatrix} \alpha_3 \\ \alpha_4 \\ \alpha_5 \\ \alpha_6 \\ \alpha_8 \end{bmatrix}$$
(B.5)

Note that the model recovers von-Mises isotropic yield model when the exponent of the model is equal to 2 and all the material coefficients become the unity.

## Appendix D. Iterations required for achieving global equilibrium for Figures 10 and 15

The discrete values of the normalized largest force residual at critical node for Figures 10 and 15 are provided as below.

Normalized largest force residual at critical node											
Iteration number		1	2	3	4	5					
Figure 10	GCPM-O	1.00	0.948	0.873	0.804	0.749					
	GCPM-N	1.00	0.317	0.101	$6.48 \times 10^{-2}$	4.76×10 <sup>-2</sup>					
Figure 15	GCPM-O	1.00	0.699 0.551		0.462	0.401					
118010 10	GCPM-N	1.00	0.268	0.018	$8.14 \times 10^{-3}$	$6.59 \times 10^{-3}$					
Iteration number		<mark>6</mark>	<mark>7</mark>	8	9	10					
Figure 10	GCPM-O	0.712	0.674	0.640	0.605	0.573					
	GCPM-N	$3.50 \times 10^{-2}$	$2.49 \times 10^{-2}$	1.75×10 <sup>-2</sup>	Conv	erged					
Figure 15	GCPM-O	0.335	0.282	0.239	0.203	0.188					
118010 10	GCPM-N	$2.75 \times 10^{-3}$	$1.74 \times 10^{-3}$	$1.14 \times 10^{-3}$	$6.92 \times 10^{-4}$	4.36×10 <sup>-4</sup>					
Iteration number		11	12	13	14	15					
Figure 10	GCPM-O	0.542	0.513	0.490	0.476	0.461					

	GCPM-N	Converged							
Figure 15	GCPM-O	0.172		156	0.139	0.123		0.109	
	GCPM-N	2.77×10 <sup>-7</sup>	$1.78 \times 10^{-4}$		1.15×10 <sup>-4</sup>	Converg		ed	
Iteration number		16	17	18	19	20	21	22	
Figure 10	GCPM-O	0.447	0.432	0.418	0.406	0.392	0.38	0.369	
Figure 15	GCPM-O	0.0956	0.0837	0.0732	0.0639	0.0557	0.0490	0.0456	
Iteration number		23	24	25	<mark>26</mark>	<mark>27</mark>	28	29	
Figure 10	GCPM-O	0.357	0.346	0.334	0.323	0.311	0.303	0.291	
Figure 15	GCPM-O	0.0426	0.0400	0.0376	0.0354	0.0335	0.0323	0.0313	
Iteration	number	30	31	32	33	34	35	36	
Figure 10	GCPM-O	0.283	0.273	0.265	0.256	0.247	0.239	0.231	
Figure 15	GCPM-O	0.0303	0.0293	0.0284	0.0275	0.0267	0.0259	0.0252	
Iteration number		37	38	39	40	41	42	43	
Figure 10	GCPM-O	0.224	0.216	0.209	Converged				
Figure 15	GCPM-O	0.0245	0.0238	0.0232	0.0226	0.0220	0.0214	0.0209	
Iteration	number	44	<mark>45</mark>	<mark>46</mark>	<mark>47</mark>	48	<mark>49</mark>	50	
Figure 15	GCPM-O	0.0204	0.0199	0.0194	0.0190	0.0185	0.0181	0.0177	
Iteration	number	51	52	53	54	<u>55</u>	<mark>56</mark>	57	
Figure 15	GCPM-O	0.0173	0.0169	0.0166	0.0162	0.0159	0.0156	0.0152	
Iteration	number	58	<mark>59</mark>	<mark>60</mark>	<mark>61</mark>	<mark>62</mark>	<mark>63</mark>	<mark>64</mark>	
Figure 15	GCPM-O	0.0149	0.0146	0.0143	0.0141	0.0138	0.0135	0.0133	
Iteration	number	<mark>65</mark>	<mark>66</mark>						

## References

- Abaqus, 2018. User's Manual (2018). Hibbit, Karlsson & Sorensen Inc,. USA.
- Baltov, A., Sawczuk, A., 1965. A rule of anisotropic hardening. Acta Mech. 1, 81–92.
- Barlat, F., Brem, J.C., Yoon, J.W., Chung, K., Dick, R.E., Lege, D.J., Pourboghrat, F., Choi,S.H., Chu, E., 2003. Plane stress yield function for aluminum alloy sheets Part 1:Theory. Int. J. Plast. 19, 1297–1319.
- Barlat, F., Gracio, J.J., Lee, M.G., Rauch, E.F., Vincze, G., 2011. An alternative to kinematic hardening in classical plasticity. Int. J. Plast. 27, 1309–1327.
- Barlat, F., Ha, J., Grácio, J.J., Lee, M.-G., Rauch, E.F., Vincze, G., 2013. Extension of homogeneous anisotropic hardening model to cross-loading with latent effects. Int. J. Plast. 46, 130–142.
- Barlat, F., Vincze, G., Grácio, J.J., Lee, M.-G., Rauch, E.F., Tomé, C.N., 2014.

  Enhancements of homogenous anisotropic hardening model and application to mild and dual-phase steels. Int. J. Plast. 58, 201–218.
- Bong, H.J., Lee, J., Lee, M., Kim, D., 2019. Identification of mechanical responses of steel sheets under non-proportional loadings using dislocation-density based crystal plasticity model. Int. J. Mech. Sci. 155, 461–474.
- Butuc, M.C., Barlat, F., Vincze, G., 2019. The formability of twinning—Induced plasticity steels predicted on the base of Marciniak-Kuczynski theory. J. Mater. Process. Technol. 116496.
- Cardoso, R.P.R., Yoon, J.W., 2009. Stress integration method for a nonlinear kinematic/isotropic hardening model and its characterization based on polycrystal plasticity. Int. J. Plast. 25, 1684–1710.

- Chaboche, J.L., 1986. Time-independent constitutive theories for cyclic plasticity. Int. J. Plast. 2, 149–188.
- Choi, H., Choi, S., Kang, S.C., Lee, M.G., 2021. Fully implicit stress update algorithm for distortion-based anisotropic hardening with cross-loading effect: Comparative algorithmic study and application to large-size forming problem. Appl. Sci. 11.
- Choi, H., Yoon, J.W., 2019. Stress integration-based on finite difference method and its application for anisotropic plasticity and distortional hardening under associated and non-associated flow rules. Comput. Methods Appl. Mech. Eng. 345, 123–160.
- Choi, Y., Han, C.-S., Lee, J.K., Wagoner, R.H., 2006. Modeling multi-axial deformation of planar anisotropic elasto-plastic materials, part I: Theory. Int. J. Plast. 22, 1745–1764.
- Chung, K., Richmond, O., 1993. A deformation theory of plasticity based on minimum work paths. Int. J. Plast. 9, 907–920.
- Chung, K., Richmond, O., 1992. Ideal forming-I. Homogeneous deformation with minimum plastic work. Int. J. Mech. Sci. 34, 575–591.
- Ding, K.Z., Qin, Q.-H., Cardew-Hall, M., 2007. Substepping algorithms with stress correction for the simulation of sheet metal forming process. Int. J. Mech. Sci. 49, 1289–1308.
- Feigenbaum, H.P., Dafalias, Y.F., 2008. Simple model for directional distortional hardening in metal plasticity within thermodynamics. J. Eng. Mech. 134, 730–738.
- Feigenbaum, H.P., Dafalias, Y.F., 2007. Directional distortional hardening in metal plasticity within thermodynamics. Int. J. Solids Struct. 44, 7526–7542.
- Geng, L., Wagoner, R.H., 2002. Role of plastic anisotropy and its evolution on springback. Int. J. Mech. Sci. 44, 123–148.
- Ghaei, A., Green, D.E., Taherizadeh, A., 2010. Semi-implicit numerical integration of Yoshida–Uemori two-surface plasticity model. Int. J. Mech. Sci. 52, 531–540.
- Gu, Q., Conte, J.P., Yang, Z., Elgamal, A., 2011. Consistent tangent moduli for multi-yield-

- surface J2 plasticity model. Comput. Mech. 48, 97–120.
- Ha, J., Kim, J.-H., Barlat, F., Lee, M.-G., 2014. Continuous strain path change simulations for sheet metal. Comput. Mater. Sci. 82, 286–292.
- Ha, J., Lee, M.-G., Barlat, F., 2013. Strain hardening response and modeling of EDDQ and DP780 steel sheet under non-linear strain path. Mech. Mater. 64, 11–26.
- Hahm, J.H., Kim, K.H., 2008. Anisotropic work hardening of steel sheets under plane stress. Int. J. Plast. 24, 1097–1127.
- Hu, Z., Rauch, E.F., Teodosiu, C., 1992. Work-hardening behavior of mild steel under stress reversal at large strains. Int. J. Plast. 8, 839–856.
- Kim, J.H., Lee, M.G., Barlat, F., Wagoner, R.H., Chung, K., 2008. An elasto-plastic constitutive model with plastic strain rate potentials for anisotropic cubic metals. Int. J. Plast. 24, 2298–2334.
- Kim, K.H., Yin, J.J., 1997. Evolution of anisotropy under plane stress. J. Mech. Phys. Solids 45, 841–851.
- Lee, E.H., 1969. Elastic-Plastic Deformation at Finite Strains. J. Appl. Mech. 36, 1–6.
- Lee, J.-W., Lee, M.-G., Barlat, F., 2012. Finite element modeling using homogeneous anisotropic hardening and application to spring-back prediction. Int. J. Plast. 29, 13–41.
- Lee, J., Bong, H.J., Kim, D., Lee, M.-G., 2020. Modeling differential permanent softening under strain-path changes in sheet metals using a modified distortional hardening model. Int. J. Plast. 133, 102789.
- Lee, J., Bong, H.J., Lee, M.-G., 2021. Return mapping with a line search method for integrating stress of the distortional hardening law with differential softening. Comput. Struct. 257, 106652.
- Lee, J., Kim, D., Lee, Y.-S., Bong, H.J., Barlat, F., Lee, M.-G., 2015. Stress update algorithm for enhanced homogeneous anisotropic hardening model. Comput. Methods Appl. Mech. Eng. 286, 63–86.

- Lee, J., Lee, M.-G., Barlat, F., Kim, J.H., 2012. Stress integration schemes for novel homogeneous anisotropic hardening model. Comput. Methods Appl. Mech. Eng. 247–248, 73–92.
- Lee, M.G., Kim, D., Kim, C., Wenner, M.L., Chung, K., 2005. Spring-back evaluation of automotive sheets based on isotropic–kinematic hardening laws and non-quadratic anisotropic yield functions, part III: applications. Int. J. Plast. 21, 915–953.
- Lee, M.G., Kim, D., Kim, C., Wenner, M.L., Wagoner, R.H., Chung, K., 2007. A practical two-surface plasticity model and its application to spring-back prediction. Int. J. Plast. 23, 1189–1212.
- Lee, S.-Y., Kim, J.-M., Kim, J.-H., Barlat, F., 2020. Validation of homogeneous anisotropic hardening model using non-linear strain path experiments. Int. J. Mech. Sci. 183, 105769.
- Lester, B.T., Scherzinger, W.M., 2017. Trust-region based return mapping algorithm for implicit integration of elastic-plastic constitutive models. Int. J. Numer. Methods Eng. 112, 257–282.
- Mánik, T., 2021. A natural vector/matrix notation applied in an efficient and robust return-mapping algorithm for advanced yield functions. Eur. J. Mech. A/Solids 90, 104357.
- Meier, F., Schwarz, C., Werner, E., 2016. Determination of the tangent stiffness tensor in materials modeling in case of large deformations by calculation of a directed strain perturbation. Comput. Methods Appl. Mech. Eng. 300, 628–642.
- Meng, C., Tang, Z., Chen, M., Peng, Q., 2018. Return mapping algorithm in principal space for general isotropic elastoplasticity involving multi-surface plasticity and combined isotropic-kinematic hardening within finite deformation framework. Finite Elem. Anal. Des. 150, 1–19.
- Miehe, C., 1996. Numerical computation of algorithmic (consistent) tangent moduli in large-strain computational inelasticity. Comput. Methods Appl. Mech. Eng. 134, 223–240.
- Nagtegaal, J.C., Rebelo, N., 1988. On the development of a general purpose finite element

- program for analysis of forming processes. Int. J. Numer. Methods Eng. 25, 113–131.
- Noman, M., Clausmeyer, T., Barthel, C., Svendsen, B., Huétink, J., van Riel, M., 2010. Experimental characterization and modeling of the hardening behavior of the sheet steel LH800. Mater. Sci. Eng. A 527, 2515–2526.
- Ortiz, M., Pinsky, P.M., Taylor, R.L., 1983. Operator split methods for the numerical solution of the elastoplastic dynamic problem. Comput. Methods Appl. Mech. Eng. 39, 137–157.
- Ortiz, M., Popov, E.P., 1985. Accuracy and stability of integration algorithms for elastoplastic constitutive relations. Int. J. Numer. Methods Eng. 21, 1561–1576.
- Ortiz, M., Popov, E.P., 1983. Distortional hardening rules for metral plasticity. J. Eng. Mech. 109, 1042–1057.
- Ortiz, M., Simo, J.C., 1986. Analysis of a new class of integration algorithms for elastoplastic constitutive relations. Int. J. Numer. Methods Eng. 23, 353–366.
- Peeters, B., Hoferlin, E., Van Houtte, P., Aernoudt, E., 2001a. Assessment of crystal plasticity based calculation of the lattice spin of polycrystalline metals for FE implementation. Int. J. Plast. 17, 819–836.
- Peeters, B., Seefeldt, M., Teodosiu, C., Kalidindi, S.R., Van Houtte, P., Aernoudt, E., 2001b.
  Work-hardening/softening behaviour of b.c.c. polycrystals during changing strain paths:
  I. An integrated model based on substructure and texture evolution, and its prediction of the stress–strain behaviour of an IF steel during two-stage strain paths. Acta Mater. 49, 1607–1619.
- Pérez-Foguet, A., Rodríguez-Ferran, A., Huerta, A., 2000. Numerical differentiation for local and global tangent operators in computational plasticity. Comput. Methods Appl. Mech. Eng. 189, 277–296.
- Polat, M.U., Dokainish, M.A., 1989. An automatic subincrementation scheme for accurate integration of elasto-plastic constitutive relations. Comput. Struct. 31, 339–347.
- Potts, D.M., Ganendra, D., 1994. An evaluation of substepping and implicit stress point algorithms. Comput. Methods Appl. Mech. Eng. 119, 341–354.

- Rauch, E.F., 1997. The stresses and work hardening rates of mild steel with different dislocation patterns. Mater. Sci. Eng. A 234–236, 653–656.
- Rauch, E.F., Gracio, J.J., Barlat, F., Lopes, A.B., Duarte, J.F., 2002. Hardening behavior and structural evolution upon strain reversal of aluminum alloys. Scr. Mater. 46, 881–886.
- Safaei, M., Lee, M.-G., De Waele, W., 2015. Evaluation of stress integration algorithms for elastic–plastic constitutive models based on associated and non-associated flow rules. Comput. Methods Appl. Mech. Eng. 295, 414–445.
- Scherzinger, W.M., 2017. A return mapping algorithm for isotropic and anisotropic plasticity models using a line search method. Comput. Methods Appl. Mech. Eng. 317, 526–553.
- Schmitt, J.H., Shen, E.L., Raphanel, J.L., 1994. A parameter for measuring the magnitude of a change of strain path: Validation and comparison with experiments on low carbon steel. Int. J. Plast. 10, 535–551.
- Seifert, T., Schenk, T., Schmidt, I., 2007. Efficient and modular algorithms in modeling finite inelastic deformations: Objective integration, parameter identification and sub-stepping techniques. Comput. Methods Appl. Mech. Eng. 196, 2269–2283.
- Seifert, T., Schmidt, I., 2008. Line-search methods in general return mapping algorithms with application to porous plasticity. Int. J. Numer. Methods Eng. 73, 1468–1495.
- Shi, B., Mosler, J., 2013. On the macroscopic description of yield surface evolution by means of distortional hardening models: Application to magnesium. Int. J. Plast. 44, 1–22.
- Simo, J.C., Hughes, T.J.R., 1998. Computational Inelasticity. Springer-Verlag.
- Simo, J.C., Taylor, R.L., 1985. Consistent tangent operators for rate-independent elastoplasticity. Comput. Methods Appl. Mech. Eng. 48, 101–118.
- Sloan, S.W., 1987. Substepping schemes for the numerical integration of elastoplastic stress–strain relations. Int. J. Numer. Methods Eng. 24, 893–911.
- Starman, B., Halilovič, M., Vrh, M., Štok, B., 2014. Consistent tangent operator for cutting-plane algorithm of elasto-plasticity. Comput. Methods Appl. Mech. Eng. 272, 214–232.

- Sun, L., Wagoner, R.H., 2013. Proportional and non-proportional hardening behavior of dual-phase steels. Int. J. Plast. 45, 174–187.
- Szabó, L., Jonas, J.J., 1995. Consistent tangent operator for plasticity models based on the plastic strain rate potential. Comput. Methods Appl. Mech. Eng. 128, 315–323.
- Tarigopula, V., Hopperstad, O.S., Langseth, M., Clausen, A.H., 2009. An evaluation of a combined isotropic-kinematic hardening model for representation of complex strain-path changes in dual-phase steel. Eur. J. Mech. A/Solids 28, 792–805.
- Tarigopula, V., Hopperstad, O.S., Langseth, M., Clausen, A.H., 2008. Elastic-plastic behaviour of dual-phase, high-strength steel under strain-path changes. Eur. J. Mech. A/Solids 27, 764–782.
- Teodosiu, C., Hu, Z., 1995. Evolution of the intragranular microstructure at moderate and large strains: Modelling and computational significance, in: Shen, S., Dawson, P.R. (Eds.), Proceedings of Numiform'95 on Simulation of Materials Processing: Theory, Methods and Applications. Rotterdam: Balkema, pp. 173–182.
- van Riel, M., van den Boogaard, A.H., 2007. Stress-strain responses for continuous orthogonal strain path changes with increasing sharpness. Scr. Mater. 57, 381–384.
- Waffenschmidt, T., Polindara, C., Menzel, A., Blanco, S., 2014. A gradient-enhanced large-deformation continuum damage model for fibre-reinforced materials. Comput. Methods Appl. Mech. Eng. 268, 801–842.
- Wi, M.S., Lee, S.Y., Kim, J.H., Kim, J.M., Barlat, F., 2020. Experimental and theoretical plasticity analyses of steel materials deformed under a nonlinear strain path. Int. J. Mech. Sci. 182, 105770.
- Wilkins, M.L., 1964. Calculation of elastic-plastic flow, Method of Computational Physics.
- Wissmann, J.W., Hauck, C., 1983. Efficient elastic-plastic finite element analysis with higher order stress-point algorithms. Comput. Struct. 17, 89–95.
- Yoon, J.W., Yang, D.Y., Chung, K., 1999a. Elasto-plastic finite element method based on incremental deformation theory and continuum based shell elements for planar

- anisotropic sheet materials. Comput. Methods Appl. Mech. Eng. 174, 23–56.
- Yoon, J.W., Yang, D.Y., Chung, K., Barlat, F., 1999b. A general elasto-plastic finite element formulation based on incremental deformation theory for planar anisotropy and its application to sheet metal forming. Int. J. Plast. 15, 35–67.
- Yoon, S.-Y., Lee, S.-Y., Barlat, F., 2020. Numerical integration algorithm of updated homogeneous anisotropic hardening model through finite element framework. Comput. Methods Appl. Mech. Eng. 372, 113449.